

NOVEL SELF-ADAPTING MICROSCALE SURFACE TEXTURES FOR
HYDRODYNAMIC LUBRICATION

Except where reference is made to the work of others, the work described in this thesis is my own or was done in collaboration with my advisory committee. This thesis does not include proprietary or classified information.

Ravi Shankar Duvvuru

Certificate of Approval:

Jay M Khodadadi
Professor
Mechanical Engineering

Robert L Jackson, Chair
Assistant Professor
Mechanical Engineering

Jong Wook Hong
Assistant Professor
Materials Engineering

George T. Flowers
Interim Dean
Graduate School

NOVEL SELF-ADAPTING MICROSCALE SURFACE TEXTURES FOR
HYDRODYNAMIC LUBRICATION

Ravi Shankar Duvvuru

A thesis

Submitted to

the Graduate Faculty of

Auburn University

in Partial Fulfillment of the

Requirements for the

Degree of

Master of Science

Auburn, Alabama
December 17, 2007

NOVEL SELF-ADAPTING MICROSCALE SURFACE TEXTURES FOR
HYDRODYNAMIC LUBRICATION

Ravi Shankar Duvvuru

Permission is granted to Auburn University to make copies of this thesis at its discretion, upon the request of individuals or institutions and at their expense. The author reserves all publication rights.

Signature of Author

Date of Graduation

VITA

Ravi Shankar Duvvuru, son of Radha Krishnaiah and Varalakshmi Devi was born on July 7th, 1982, in Cuddapah District in India. He got his Bachelor of Technology degree from Sri Venkateswara University, Tirupati, INDIA in 2005. He joined the Masters program in the department of Mechanical Engineering at Auburn University in August 2005. His research interests include contact of surfaces, surface texturing and thin film lubrication.

THESIS ABSTRACT

NOVEL SELF-ADAPTING MICRO SCALE STRUCTURES FOR HYDRODYNAMIC LUBRICATION

Ravi Shankar Duvvuru

Master of Science, December 17, 2007
(B.Tech, Sri Venkateswara University, 2005)

97 Typed Pages

Directed by Robert L. Jackson

The tribological performance of a lubricated surface depends largely on the ability of the surface to maintain a sufficient film thickness under high loads. One way of improving the performance is to modify the surface by inducing changes in the geometry of the surface. This work deals with modeling, creating and testing novel adaptive microscale surface geometries to improve the tribological performance in terms of load carrying capacity.

Numerical methods are used to model and simulate the performance of these surfaces. Coupled mechanisms involving elasticity theory and the Reynolds equation were solved for the values of pressure and load acting on the surface. Parametric studies were also performed by varying the input conditions and variables involved. The results were nondimensionalized by using a standard normalization scheme throughout the work to make them easy to compare and deduce the trends. Efforts were made to optimize the geometry of the surface to improve the performance in terms of increased load carrying

capacity. Numerical results show that the adapting surfaces are able to increase the effective stiffness of the hydrodynamic film in comparison to conventional textured surfaces. It was theoretically also shown that adapting microscale structures perform better in terms of load carrying capacity for the same amount of film thickness. This is due to the increase in the fluid film stiffness of the adapting or smart surfaces which change their geometric profile according to the applied load.

The proposed self-adapting surfaces were fabricated using microfabrication techniques and a test rig to characterize the surfaces was designed and built. The self adapting or smart surfaces were made of Polydimethylsiloxane (PDMS) which is a polymer of silicon. PDMS was chosen for its ease of fabrication and design. PDMS has also the property of optical transparency which helps in viewing the surface behavior when in contact through a microscope. The test rig consists of a load cell to measure the amount of load acting on the surface due to the pressure exerted by the fluid. A variable-speed motor is also part of the rig which can be used to vary the velocities to simulate the real time conditions experimentally. The film thickness too can be controlled accurately at the microscale level with the help of micrometer stages. A microscope was planned to be used to view the whole process and observe phenomenon like cavitation for the better understanding of the surface behavior. Although the test rig was built, due to paucity of time the experimental measurements could not be conducted.

ACKNOWLEDGMENTS

I would like to thank my advisor, Dr. Robert L Jackson for helping me carry out this work. His unstinted support and patience when things were not going smoothly were the pillars of this work. He has been a very good advisor both academically and personally. Doing research under him was a good learning experience which will be useful throughout my life. His tutelage enabled me to develop a strong work ethic and a penchant for research. He will continue to remain as the person whom I look up to when in doubt. Thanks are also due to Dr. Jay M Khodadadi for agreeing to be a part of my committee. His courses in fluid mechanics have increased my understanding of the subject and are some of the best classes I ever took. I would like to extend my appreciation and thanks to Dr. Jong Wook Hong for all the help in preparing the specimen for experimental testing.

Thanks to Manoj Mahajan, Lei Jiang, William Wilson Everett, Santosh Angadi, Chandru Periaswami, and Vijay Krithivasan, Sachin Jambovane for their help at various stages of my project. I also would like to thank Aditya Konduru, Phani, Raghu Kishore and all the people of Telugu Community whom made my stay at Auburn a pleasant one.

I would like to show my gratitude to my parents who made many sacrifices to help me reach this stage. I also thank my sisters who were always a great source of emotional support. I dedicate this work to my family without whom, I would not have made it so far.

Style manual or journal used Microsoft Office Word and references cited as per Tribology transactions.

Computer Software used MATLAB 7.0.4, Microsoft Office Power Point 2003, Microsoft Office Excel 2003 and Solid Edge.

TABLE OF CONTENTS

LIST OF FIGURES	xi
LIST OF TABLES	xiii
NOMENCLATURE	xiv
INTRODUCTION	1
1.1 Overview	1
1.2 Motivation.....	5
LITERATURE REVIEW	8
NUMERICAL MODELING	14
3.1 Numerical Methodology	14
3.2 Principle of Superposition.....	19
3.3 Geometrical constants employed in the numerical modeling.....	24
NUMERICAL RESULTS	25
4.1 Mesh Convergence.....	27
4.2 Pressure Profile	28
4.3 Pressure Profile for various film thicknesses.....	30
4.4 Pressure Profile for various foil thicknesses.....	31
4.5 Deflection profile for the bench mark case.....	32
4.6 Deflection profiles for various film thicknesses	33
4.7 Film Thickness Profile for the benchmark case.....	34
4.8 Defining the yielding limit.....	36

4.9 The effect of film thickness and velocity on Average pressure.....	38
4.10 The effect of film thickness ratio and foil thickness on dimensionless load capacity.	40
4.11 Static vs. deformable case.....	43
4.12 Comparison of film stiffness for deformable and static cases:.....	44
4.13 Variation of load with foil thickness value, g^*	45
4.14 Variation of load with foil thickness for a film thickness value of 3 μm :.....	47
4.15 Variation of load with foil thickness for a film thickness value of 7 μm :	48
4.16 Plot of Dimensionless load for various length ratios:.....	49
EXPERIMENTAL METHODOLOGY	51
5.1 Surface Micro-Fabrication	51
5.2 PDMS chip preparation process.....	52
5.2.1 Preparation of mold:	53
5.2.2 Preparation of the PDMS specimen:.....	54
5.5 Experimental setup.....	57
5.6 Experimental Scheme	61
CONCLUSIONS	64
6.1 Scope for future work	66
REFERENCES	67
APPENDIX A.....	72
MATLAB CODE FOR GENERATING THE PRESSURE PROFILE	72
APPENDIX B	77
MATLAB CODE FOR GENERATING THE DIMENSIONLESS LOAD PROFILE	77

LIST OF FIGURES

Figure 1.1: Figure showing various regions of lubrication (Stribeck curve).....	2
Figure 1.2: Schematic of Self adapting step bearing – (Jackson, 2005).....	5
Figure 1.3: Response of static and self adapting step bearing to a sinusoidal varying applied load.....	6
Figure 3.1: Schematic of elastic self-adapting surface using deformable bridges to cause controlled deformation.....	15
Figure 3.2: Current self- adapting surface for hydrodynamic lubrication	16
Figure 3.3: schematic of the beam section used to calculate the deflection values	17
Figure 3.4: Application of principle of superposition.....	19
Figure 3.5: Flowchart explaining steps in numerical modeling.....	22
Figure 4.1: Plot showing the variation of dimensionless load used for mesh convergence	28
Figure 4.2: Plot of the Pressure profile over the section for the benchmark case.....	29
Figure 4.3: Plot of Pressure profiles for various film thicknesses	30
Figure 4.4: Plot of Pressure profiles for various foil thicknesses	32
Figure 4.5: Deflection profile for the bench mark case of 5 microns.....	33
Figure 4.6: Variation of deflection with film thickness.....	34
Figure 4.7: Variation of film thickness along the textured surface.....	35
Figure 4.8: Variation of dimensionless load carrying capacity with film thickness.....	38

Figure 4.9: Plot of average pressure as a function of thickness for various velocities	39
Figure 4.10: Plot of dimensionless load as a function of film thickness ratio for various velocities	40
Figure 4.11: Figure with dimensionless load variation for various foil thicknesses	42
Figure 4.12: Comparison of the deformable surface with the non deformable	43
Figure 4.13: Plot of Non dimensional film stiffness and dimensionless film thickness...	45
Figure 4.14: Variation of dimensionless load with foil thickness ratio for the benchmark case of 5 μm	46
Figure 4.15: Variation of dimensionless load with foil thickness for a film thickness of 3 μm	47
Figure 4.16: Plot of dimensionless load and foil thickness for film thickness of 7 μm ..	48
Figure 4.17: Plot of optimum foil thickness for various initial film thicknesses.....	49
Figure 4.18: Plot of Dimensionless load for various length ratios.	50
Figure 5.1: Schematic flows of the surface micro fabrication with multilayer soft lithography	52
Figure 5.2: Figure describing the steps in the preparation of Mold surface	55
Figure 5.3: Microscopic view of the mold.....	55
Figure 5.4: Figure describing the steps in the preparation of PDMS surface	56
Figure 5.5: Experimental setup diagram showing various components used.....	57
Figure 5.6: Design view of the bowl which houses the two surfaces to be tested.....	59
Figure 5.7: Design and photographic view of the slide holder which holds the PDMS specimen	60
Figure 5.8: Photographic view of the experimental setup	63

LIST OF TABLES

Table 1: Properties of the PDMS material.....	23
Table 2: Constants used in Numerical modeling as parameters	24
Table 3: Input parameters for the benchmark case	25

NOMENCLATURE

c	Area on which pressure is acting (m^2)
D	Deflection (μm)
E	Modulus of elasticity (Pa)
g	Foil thickness (μm)
g^*	Dimensionless foil thickness (g/rl)
H	Initial or minimum thickness (μm)
\bar{h}	Film thickness for a self-adapting step bearing (m)
h_0	Minimum film thickness for a self-adapting step bearing (m)
h^*	Dimensionless film thickness (h/rl)
I	Moment of inertia (m^4)
l	Length of the section (m).
N	Viscosity (Pa ·sec)
P	Force due to pressure acting (N).
p	Pressure (N/m^2)
p^*	Dimensionless pressure ($pl/6nu$)
P_i	Initial load (N)
r	Length ratio (Deformable length/Total length)
s	Number of nodes
S_h	Inset height (m)

u	Velocity (m/sec)
W	Dimensionless load ($Pl/6nu$)
w	Width of the section (m).
X	Distance from the end of previous section (m)
σ	Maximum allowable stress (MY/T)

CHAPTER 1

INTRODUCTION

Interaction of opposing surfaces when in contact is the cause of friction and wear, which is detrimental to the components of the surfaces. There is a need to improve the efficiency of the system or components without affecting the amount of friction or wear. The current work looks into a set of surfaces which can be termed as “smart or self-adaptive surfaces” and their primary function is to adapt at micro (or) nanoscale level, thereby improving the performance by increasing the load carrying support. The proposed surfaces will find use in the vastly expanding micro electro mechanical systems (MEMS) industry where precision control is required to a higher degree. The self-adapting surfaces mentioned in this work are easy to manufacture by the existing micro fabrication methods. The scope of this work would be to manufacture the proposed surfaces with different materials.

1.1 Overview

The amount of friction occurring between two lubricated surfaces is characterized by the Stribeck curve with the amount of friction reducing when one moves from boundary and mixed lubrication to full-film lubrication (FFL). In FFL the two surfaces are out of contact and separated by a fluid film between them. Then virtually no wear will occur and the friction too is very low.

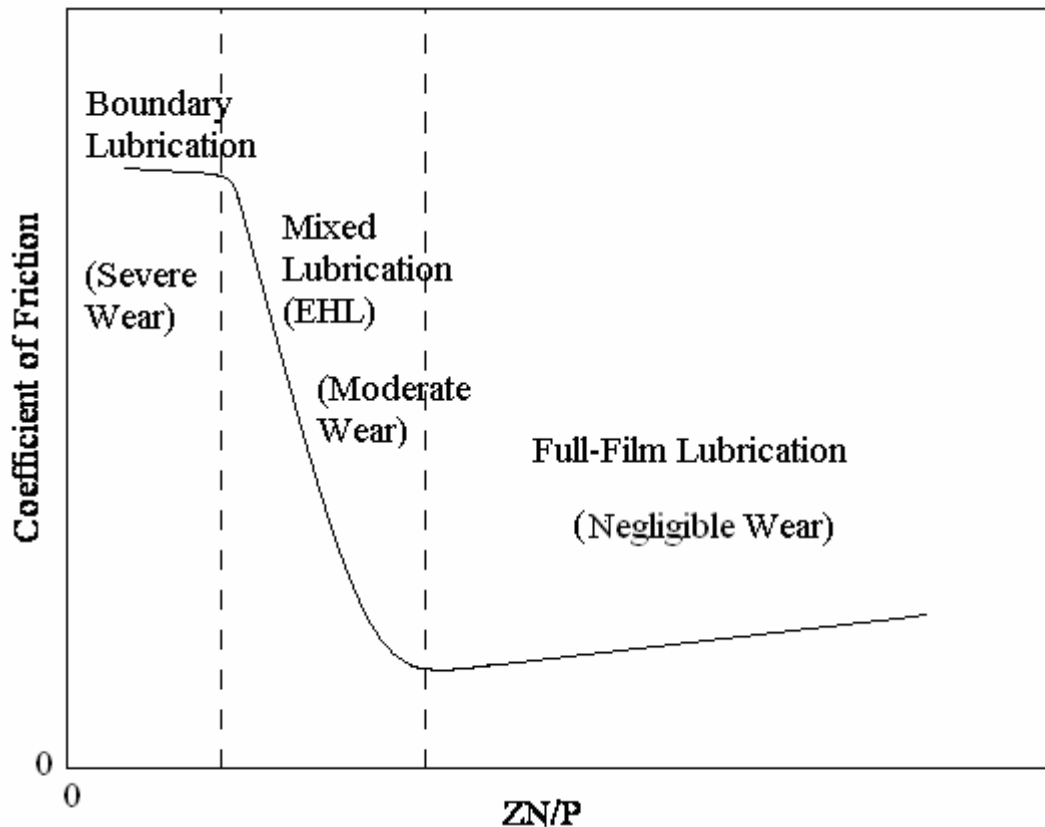


Figure 1.1: Figure showing various regions of lubrication (Stribeck curve)

The above curve is used to differentiate the types of lubrication ranging from full film to boundary or dry lubrication. Of the three types the most desirable is the extreme right full film lubrication where there is negligible wear and very low coefficient of friction due to absence of contact between the surfaces. In this region of the Stribeck curve the rotational speed and viscosity are high enough to generate hydrodynamic lift to overcome the pressure exerted by the load and separate the surfaces with a thin film of lubricant thereby ensuring no contact between the opposing surfaces. Now, if the bearing is operating under high loads and/or at low speeds, it might be located in either the mixed

or boundary lubrication regime where contact might occur between the surfaces. Then contact occurs between the asperities of the two surfaces and can increase the wear and friction drastically. In these regions some hydrodynamic lift is still produced, but it is not sufficient enough to maintain a full film between the surfaces. The proposed work is aimed at making the surfaces operate in full film lubrication region so that there would be negligible wear and overall better performance. Thus, one of the goals of this work is to extend the region of full film lubrication to the left so that even at low values of viscosity and velocity there would be less wear.

For two lubricated surfaces in close proximity, the microscale surface profiles have a very important role to play. By inducing controlled variations in the microscale profile of the surface, the performance can be improved by providing additional hydrodynamic load support. Recently, extensive research [1-25] has been made to optimize these surfaces and to characterize their performance. This led to many advances like micro textured surfaces [1-4], Laser Surface Texturing (LST) [4-25], which actually improve lubrication by expanding the hydrodynamic lubrication regime of the Stribeck curve.

Attempts [26] have been made to control the surface texture by variation of the pressure in pockets below the surface. The pressure then deforms the surface above it. The key here is flexibility. What if a surface is manipulated in such a way that the limitations (or) the critical values of the operating parameters can be extended significantly? Here the adaptive surfaces considered in this work come into play. Research on adaptive surfaces has been scarce. Adaptive surfaces have been designed by placing sensors at strategical positions which collect the real-time data and use this to

change the surface by controlling pressure in specially built pockets under the surfaces and change the way the surface behaves [26]. But the usage of computer control makes this unreliable, costly and with limited application. So, the need arises for the development of independent “adaptive surfaces” which without the help of the external media will be able to sustain a full film thickness for a very large range of loads acting on it.

Efforts have been made in this work to numerically model a novel micro surface texture so that insight is given as to what to expect in the experimental stage and in actual operation. The results can also be compared and correlated with their conventional smooth and textured counterparts in the experimental stage. Possible differences between the numerical and experimental results would provide some insights or fallacies in either approach. Also, modeling would provide a platform which can be used as a stepping stone for further work in this area. This work numerically and experimentally studies novel self- adapting surfaces that operate via the deformations of micro scale structures. The surfaces in this work are self-optimizing for varying applied loads, but they do so without any external control.

This work makes an attempt to create a prototype surface test its usage and tries to characterize the advantages of it over a conventional surface used. A numerical model which uses the Reynolds equation to predict pressures as a function of the surface geometry will be prepared first and the predicted performance elucidated by varying parameters like film thickness, velocity (sliding) and comparison of a deformable to an un-deformable surface. The surface will be fabricated using MEMS techniques and will

be tested using specially designed testing equipment. However, the experimental portion of the research was not completed during the course of this work.

1.2 Motivation

The main motivation for the present idea stems from the work done by Wood et al [25], “Self- adapting step bearings” by Jackson [27]. As in the Fig. 1.2 below, the self adapting step bearings are based on the design that when load is acting on the bearing the surface profiles change to achieve an optimal behavior. This is done by placing a spring (see Fig. 1.2) placed between a translating step inset and the bulk bearing material to control the height of the inset in a sliding step bearing geometry. If the spring is selected with a suitable stiffness, the geometry results in a step bearing that adapts to changes in applied load. This results in a bearing which can maintain a constant film thickness in spite of changes in applied load.

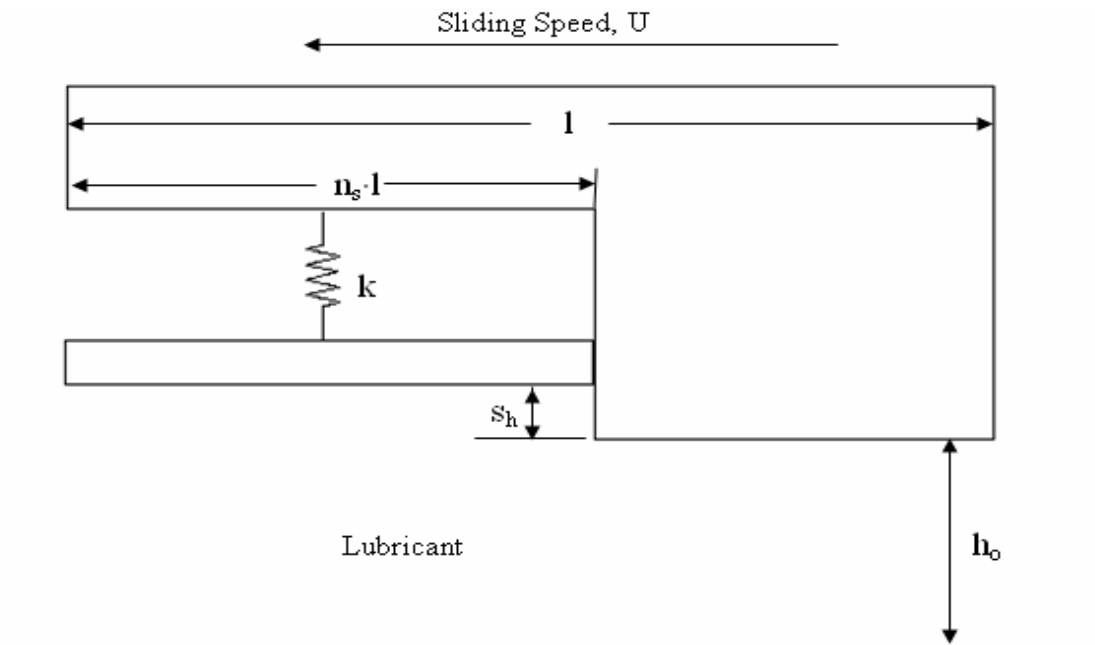


Figure 1.2: Schematic of Self adapting step bearing – (Jackson, 2005)

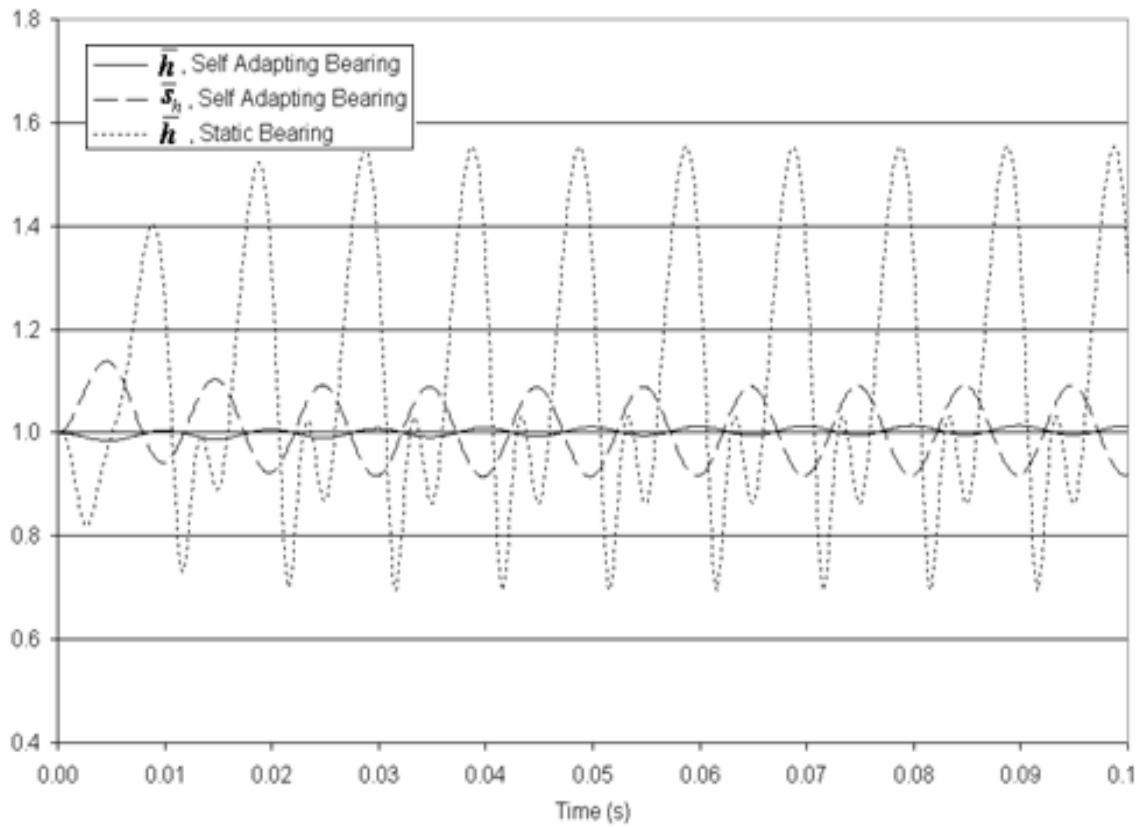


Figure 1.3: Response of static and self adapting step bearing to a sinusoidal varying applied load

The plot shown in Fig.1.3 explains the performance of the self- adapting step bearing. Notice the very little variation of the film thickness (h - self adapting bearing) when compared to a static bearing. This proves the concept that adapted bearings adjust their surface geometry so as to maintain a constant film thickness constant and carry some very good advantages over static bearings.

However, technologies like the above said are needed in today's world especially in MEMS, hard drive disks and mechanical seals where precision control is very important and it pays to control the film thickness. So there arises a need to develop

bearing surfaces through which we can control the film thickness precisely in spite of changes in applied load. All this being said and done the precision control should not come at a cost of integrating the surfaces with some miniature electronic equipment which sense the conditions and send data to a computer which uses the data to alter the surface. This may pose reliable problems and possess limitations pertaining to the areas of application.

The proposed work would especially be of use in Nano and Micro-scale precision systems like read/write heads of the hard drives where the need of maintaining constant film thickness is present. Although tilted pad bearings are a step in this direction they optimize for varying film thicknesses not for loads.

The need for a bearing surface which could self-optimize to the variations in the applied load and still maintain a near constant film thickness is prevalent in the modern day miniature scale technologies. Furthermore the surface in this work does not need any external control of any form which makes it purely mechanical. This work is an effort to create a surface with the above mentioned qualities.

CHAPTER 2

LITERATURE REVIEW

Surface texturing has been looked upon as a way to improve the performance of the surface in terms of load carrying capacity, better friction characteristics, wear resistance and improved lubrication. Although this field has gained significant interest in recent times the origination of the idea dates back to a few decades when texturing in the form of micro-asperities [1] has been proposed to improve the performance in a sliding contact by acting as micro-hydrodynamic bearings. Another instance of surface texturing was the honing of cylinder liners [2].

Etsion and Burstein [3] proved in 1996 that performance of a mechanical seal can be improved by the presence of equally spaced micro dimples on one of the faces of the seal. This was followed up [4] with some experimental work to show the improved performance and an effort was made to optimize the geometry of the micro-textures. The reason for the better performance of the seals with textures was due to the increase in the stiffness of fluid film.

Texturing the surfaces was also proposed to be a friction reducing phenomenon in the reciprocating automotive components. Ronen et al [5] presented an idea where the piston rings were textured to contain micro-pores that act as hydrodynamic bearings to improve hydrodynamic lubrication. This too was followed up experimentally [6] and it was proved in practical terms that surface texturing reduces friction in reciprocating

automotive components. Applications of texturing were also found in hydrostatic mechanical seals [7] and parallel thrust bearings [8]. All the above mentioned [3-8] processes create surface textures by laser surface texturing [LST]. Although LST has many advantages in being quick, easy and very effective [9] it has its share of disadvantages [10] as well, like heating of the surrounded parts, splattering etc. The most important thing is that surface texturing can be used to the advantage in reducing friction and increasing load carrying capacity.

Surface texturing also helps in improved performance by a process called secondary lubrication [11] wherein the fluid trapped in the textures can act as a secondary source of fluid when in need of lubricant under extreme conditions. This would be important when operating on left side of the Stribeck curve (see Fig. 1.1). These textures can also act as wear reservoirs by entrapping the wear particles which will result from the asperity contact. But the most important advantage is probably the increased load support generated due to the textures and the increase of film stiffness.

Laser surface texturing has been tested on various materials like steel with chromium coatings [10-11], Tungsten carbide and silicon carbide [SiC]. In all cases it appeared to improve the lubrication and increasing the load carrying capacity. The three main parameters which affect the performance of a laser textured surface are the diameter, depth and area density. According to [12], the shape of the texture does not play a major role in generating the optimum load carrying capacity, but what is important is the ratio of the texture depth to the diameter. The lasers used until now are CO₂ and Nd: YAG types [13]. It has been proved that the LST is effective not only in liquid lubrication (incompressible) but also in dry gas seals too. The process of LST is done by

exposing the surface to a pulsating laser beam which creates many micro dimples. The frequency of micro dimples is controlled by controlling the area density (total dimple area/total surface area).

The ground breaking work in LST is done by Etsion et al [14-21]. Though many people are presently using laser ablation process to produce surface textures, it was Etsion and his colleagues who paved the way by modeling analytically the dimples and then following it up with experimental testing and then giving out an optimal geometry of the texture which gives highest possible load carrying capacity. He also explored texturing in mechanical seals, thrust washer bearings and reciprocating automotive components.

Although there are many good things about LST, the process has its limitations. Some of them are:

- 1) Texturing by exposing to laser may cause splattering of the material in the neighboring areas thereby affecting the roughness or smoothness of the surface so a surface finishing process needs to be performed after laser treatment so as to make the surface even with respect to the surroundings.
- 2) In some cases the laser can be so powerful that it develops cracks in the surrounding regions thereby causing a decrease in the hardness of the material.

Of course with the current technology growth it might not be long before these minor limitations will be overcome and a standardized process will be adopted to take advantage of the improvement in tribology properties this process offers.

Although LST has been discussed in detail it does not mean that it is the only method of creating surface textures. Researchers world wide have tried several other

methods to create textures. Costa and Hutchings [22] used photo chemical etching to create textures on steel surface and they used to test this surface under reciprocating sliding conditions. Wang et al [9-10] used reactive ion etching to create the Micro pits (textures) in SiC thrust bearing sliding in water. The processes maybe different but the purpose remains the same, to improve the tribological performance of surfaces when in contact. From their experiments X.Wang et al [9-11] conclude that:

There exists an optimum range for the pit geometry factor, depth-diameter ratio (h/d), and the distribution factor, pit area ratio r , where the critical load can to cause failure can be improved to be at least twice that of a conventional surface. This is almost the same to the conclusion made by Etsion et al [14-20], the only differences being the method of creating the texture and the material used to test.

Another application of surface texturing is that it can be used to overcome stiction and adhesion in precision devices [23]. This advantage is presently commercially explored in all the hard disk drives [24-25] where the film height is only a few nanometers and the maintenance of constant film height is necessary for the smooth operation of the disk drive. However, the texturing is controlling different mechanisms of adhesion and stiction, while the current work is mainly interested in hydrodynamic lubrication.

Most of the above techniques are only experimental and the optimal geometries in each case vary significantly because they were arrived at by using trial and error technique. Lack of comprehensive numerical modeling is because of the difficulty in coming up with analytical models for such a complex process involving many parameters

and it is not possible to gage the contribution of each of these parameters to the overall performance.

Baroud [26] and his colleagues explored the idea of embedding sensors and actuators in the hydrodynamic bearing so that controlled micro structures would evaluate the surfaces and adapt the surface accordingly. By using micron scale actuators to actively control the thrust and drag forces on a slider bearing they could improve the performance of a bearing by more than 100 percent during operation, increasing the bearing's range of operation. Although this looks very interesting and promising the defect with such systems is that embedding or integrating electronic devices into the hydrodynamic bearings limits their operation to certain applications and environments only. Such approaches require computer control to optimize the surfaces based on real time data collected from strategically placed sensors. This increases the cost and limits the number of applications where such a complex system can be installed and used. Placing of the sensors and actuators might also actually affect the reliability of the surface. However, the above mentioned idea provides some very good insights for the present work i.e. adaptive surface can be used to create smart bearings where the surface adapts depending on the load acting on it. This paves the way for creation of self optimizing surfaces that by adapting themselves to the operating conditions also result in better performance for a wide range of applications.

The present work is also very closely related to the idea of “Self Adapting Step Bearings” by Jackson [27] who showed theoretically that by placing a spring with a suitable stiffness at the inset of a step bearing, that the initial or minimum film thickness can be maintained constant in spite of load variation. This is due to the adapting

mechanism of the spring that maintains the film thickness constant when load is applied. The same principle is used in this work to create adapting surfaces which attempt to maintain a constant film thickness even though the load varies (i.e. the film stiffness is increased). The spring in the step bearings is being replaced by a thin foil which performs the same function of the spring i.e. adapt to increase the stiffness of the film. The present work can be termed as a practical version of Jackson's work because in reality the selection and design of the spring with the suitable stiffness is a difficult task. The present work is an effective way of using the surface texturing and the adaptive control of surfaces to create a new set of bearing surfaces known as smart bearing surfaces or self optimizing surfaces. The surfaces discussed in the present work deform mechanically into the surface textures or grooves beneath due to the load acting on them exerted by the fluid pressure. The deformation of the surfaces is therefore controlled by the amount of fluid pressure acting. The entire process is a purely mechanical one and can be used in any application regardless of the operating conditions and the environmental surroundings.

CHAPTER 3

NUMERICAL MODELING

3.1 Numerical Methodology

In the current work, the self-adapting micro textures will be modeled as being located on one surface that is sliding in close proximity to another perfectly flat surface. In this case the deformation of the structure is dependent on the fluid pressure of the lubricant, while the fluid pressure is dependent on the deformation or geometry of the structure, making the mechanisms coupled. The numerical model of the self- adapting surfaces will be constructed considering these coupled effects and the geometries shown in Fig. 3.1. It will predict the load support of the surfaces with the micro surface textures and also help to design the surface structure geometry for prototype surfaces which will later be fabricated for the experimental work. The Reynolds equation will be used to consider the fluid dynamics of the lubrication. The classic Reynolds equation [41] for thin film lubrication is:

$$\frac{\partial}{\partial x} \left(\frac{\rho h^3}{\mu} \frac{\partial p}{\partial x} \right) + \frac{\partial}{\partial z} \left(\frac{\rho h^3}{\mu} \frac{\partial p}{\partial z} \right) = 6U \frac{\partial(\rho h)}{\partial x} \quad (3.1)$$

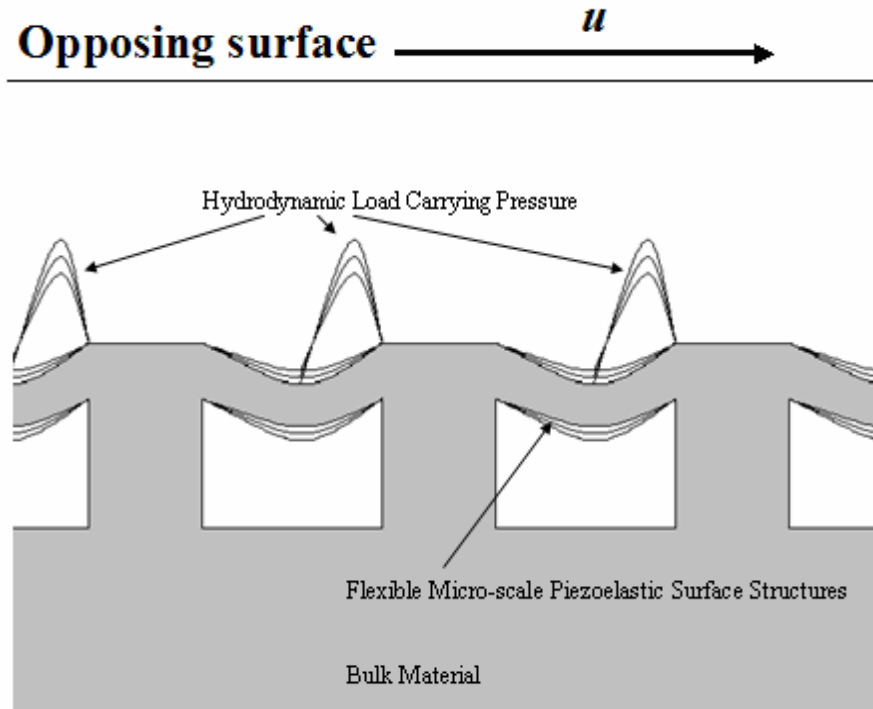


Figure 3.1: Schematic of elastic self-adapting surface using deformable bridges to cause controlled deformation

where h is the film height, p is the fluid pressure, μ is the viscosity, and U is the relative velocity between the sliding surfaces in the direction of sliding, x . The Reynolds equation is a simplified version of the general Navier-Stokes equations for thin films of fluids between sliding and squeezing surfaces. The Reynolds equation will be used to solve for the fluid pressures on the self-adapting surface as a function of the deformed surface geometry. The pressure is also dependant on the sliding and normal velocity between the surfaces and the lubricant viscosity. The current model makes the following assumptions in Numerical Modeling:

1. Infinitely long (neglecting side leakage)
2. Incompressible fluid

Taking these assumptions to consideration and simplifying the Reynolds equation leads to:

$$\frac{\partial}{\partial x} \left(h^3 \frac{\partial P}{\partial x} \right) = 6\mu U \left(\frac{\partial h}{\partial x} \right) \quad (3.2)$$

The Reynolds equation is discretized using the finite difference method (FDM), resulting in a set of linear equations. These equations are then solved iteratively using the Gauss-Seidel method to provide the fluid pressures. The fluid pressure is also numerically integrated over the surface area to predict the load support produced by the self- adapting surfaces. The Simpson's method is used for numerical integration of pressure over the length to provide force or load support.

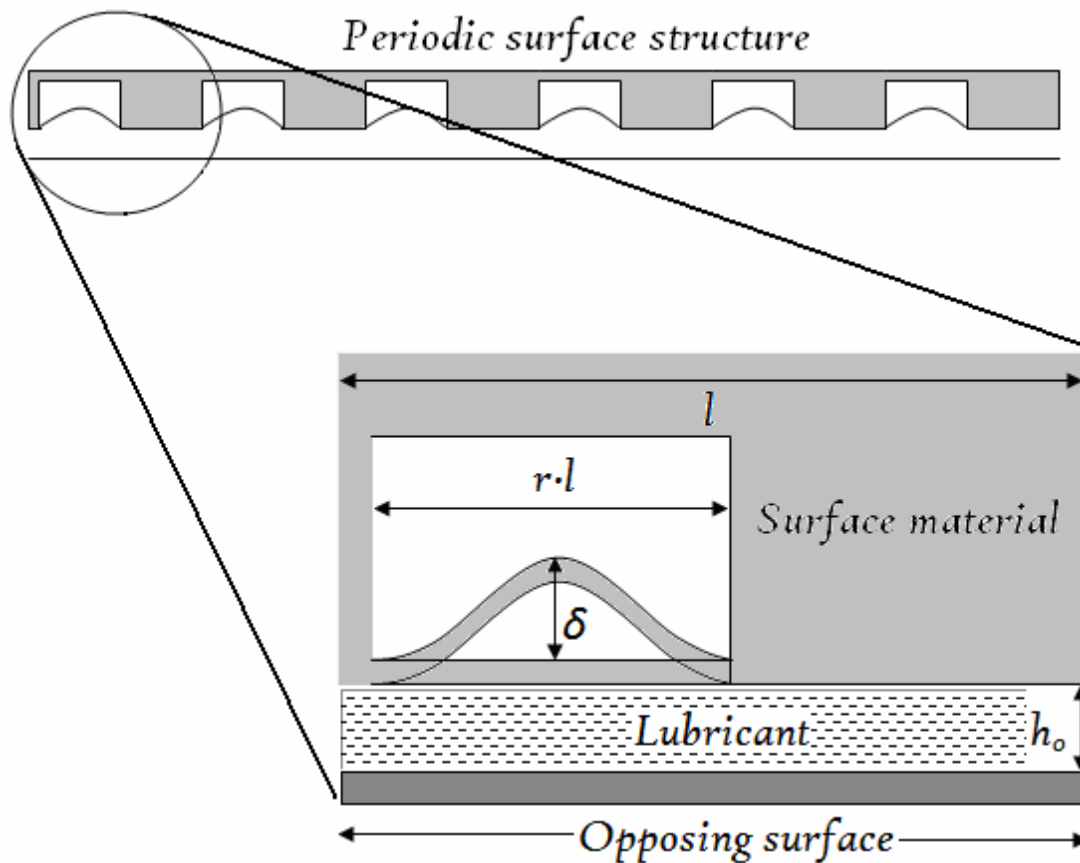


Figure 3.2: Current self- adapting surface for hydrodynamic lubrication

Since the grooves are equally spaced on the surface the pressure distribution across the grooves can be assumed to be the same and periodic so considering symmetry the numerical modeling is done for just one groove and the resulting load support can be multiplied with the number of grooves to give the load support for the entire specimen. At the $X=0$ and $X=l$ boundaries a cyclic condition is thus applied.

The surface is divided into a number of sections which are represented by nodes. The deflection of the surface under load applied is calculated at these nodes. The current scenario is approximated using a fixed-fixed beam with a point load acting on it. The entire section is divided into two parts, i.e. the deformable and the stiff region. The deflection is fixed to zero in the stiff region. The Euler-Bernoulli beam theory is used to calculate the deflection at the nodes due to the load applied. The load acting is given by the pressure at the node by multiplying with the area of the node

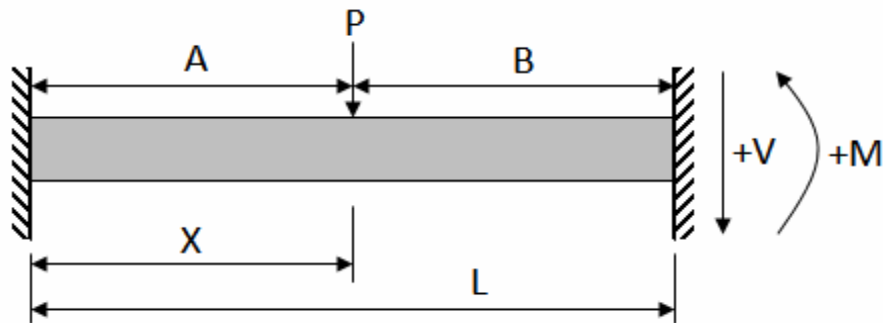


Figure 3.3: schematic of the beam section used to calculate the deflection values

Based on the Euler-Bernoulli beam theory [43], the formula used to calculate the deflection at the nodes is:

$$\delta = \frac{P}{6EI} \left[\frac{B^2 x^3}{(r.l)^3} (r.l + 2A) - \frac{3AB^2 x^2}{(r.l)^2} - (x - A)^3 \right] \quad (3.3)$$

Where

δ = deflection

E = Young's modulus

I = moment of inertia

L = length of the beam

P = load acting on the beam

r = Length ratio (deformable region length/total length)

A = distance to the point of load acting from left

B = distance to the point of load acting from right

The pressure acting on the surface is approximated by a series of point loads acting on the surface. These loads when divided by areas on which they are acting will give the pressure acting on the surface. This is done by the principle of superposition also known as Influence coefficients which is illustrated in the Fig.3.4.

3.2 Principle of Superposition

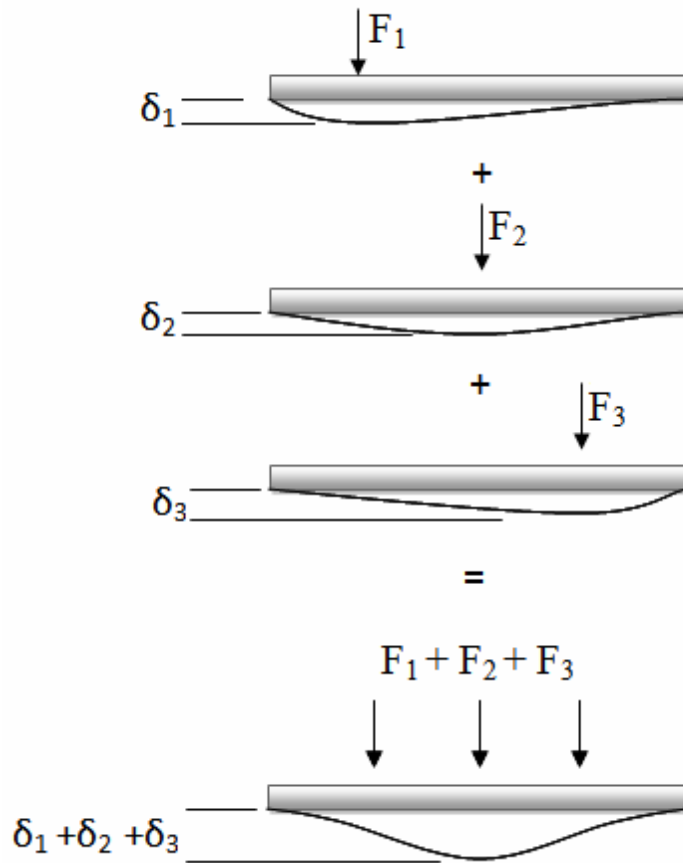


Figure 3.4: Application of principle of superposition

The deflections resulting from the fluid pressure profile predicted by the Reynolds Eq. are calculated using the superposition method. Firstly, the load is assumed to be acting on one node, the deflections of all nodes due to the load acting on that node are calculated. Then the load on the next node is calculated and again the deflections at all nodes due to the load are calculated. The process repeats itself until deflections at all

nodes due to load acting on all nodes are calculated. Then the deflections are summed up at each node to give an estimate of the total deflection.

The film thickness at each node is the sum of the initial film thickness and the deflection at the corresponding node. The resulting film thickness values are used to calculate pressure by being substituted into the Numerical solution of the Reynolds Equation.

The pressure is calculated at the first node by using the pressure value of the last node and the same process is employed when calculating the pressure at the last and final node using the pressure value at the first node. This process results in satisfying a periodic boundary condition at both ends. The nodes at which pressures fall below zero due to cavitation are made equal to zero i.e. the cavitation effect is taken care of via the Reynolds boundary condition. This process iteratively calculates pressure at each node through the Gauss Seidel method. A suitable over relaxation factor has been employed to speed up the convergence.

This load is divided into point loads on each node and the deflection is calculated again due to the load acting by the same superposition method discussed earlier. After calculating the deflection values for a second time, these are compared as a convergence criterion. If the normalized difference between the successive deflections is less than the convergence criterion then the solution is considered complete. For this work the convergence criteria is set to 10^{-5} . These deflection values are then used to calculate values of film height (h) by the equation:

$$h = h_0 + (\delta)_{\text{at the node}} \quad (3.4)$$

The new values of h are used to give values of pressure at the nodes when substituted into the numerical solution of the Reynolds Equation. The above methods are coupled through their boundary conditions and so they must be satisfied simultaneously. As described this is done by use of an iterative numerical process. This process is better explained as a flowchart in fig. 3.5. The results of the numerical model will then be used to perform a parametric study of the surface geometrical dimensions, material properties, and performance under various conditions. This study will improve the understanding of the surface performance and predict which types of surfaces and particular surface parameters produce the most feasible self- adapting surfaces.

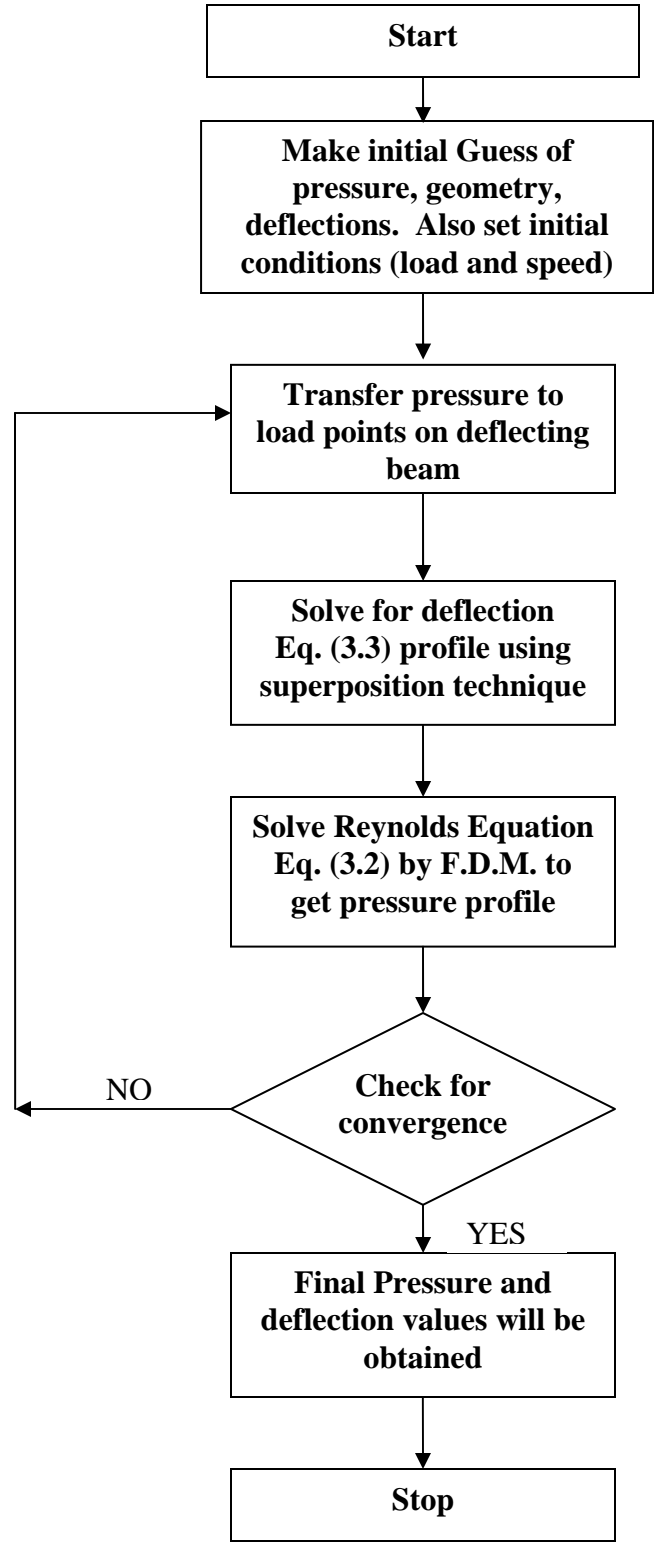


Figure 3.5: Flowchart explaining steps in numerical modeling

It should also be mentioned that the modeling has been done keeping in view of the material that will be used for the experimental. More details are available on the ensuing chapter on Experimental work. After considering the available resources and the ease of fabrication and various other factors it was decided that Polydimethylsiloxane (PDMS) presents itself to be a suitable material for fabricating the micro textures and testing them experimentally. The reasons for choosing the above said material are

1. Ease of manufacture
2. Optical transparency
3. Low cost

Of the above advantages, optical transparency is important, because by the virtue of this property, the total experimental setup can be designed in such a way that the adapting or the optimizing of the surface can be viewed with the help of interferometry techniques or by an optical microscope. One more important advantage of the PDMS is that design changes can be made easily. The preparation time of a specimen is roughly a day which can be termed neither short nor long.

The properties of the PDMS obtained from MIT properties of materials [45], which were used in the numerical modeling are given in Table 3.1.

Table 3.1: Properties of the PDMS material

Property	Value
Young's Modulus	0.8 MPa
Poisson Ratio	0.5
Tensile Strength	2.24 MPa

The young's modulus is used when calculating the deflection values by using beam theory and the tensile strength is used to arrive at a value of critical pressure to define the yielding limit beyond which the surface plastically deforms (considered as failure). See results in chapter 4 for more information.

3.3 Geometrical constants employed in the numerical modeling

The values of the geometrical constants used in the numerical model are shown in Table 3.2. These are the values used for the bench mark case. A parametric study was made by varying one variable at a time.

Table 3.2: Constants used in Numerical modeling as parameters

Properties	Value
Length of the Surface	200 μm
Width	0.02 m (2 cm)
Viscosity	$0.8592 \cdot 10^{-3}$ Pa·Sec
Velocity	7.5 m/s
Number of Nodes	160

The numerical modeling was done using MATLABTM and the processing times varied from 1 to 8 hours for most cases. A sample of the code can be found in the Appendix.

CHAPTER 4

NUMERICAL RESULTS

The Numerical methodology used in this chapter was discussed in chapter3 in detail. In this section the numerical results are presented and thoroughly discussed. The important output parameters in the present work are pressure, deflection, film thickness, and load carrying capacity. The results are normalized to give a better perspective and help in comparing the values for different cases and conditions.

The numerical simulations were performed first for a benchmark case and then subsequently each one of the parameters were varied individually while keeping the others constant performing a parametric study. The conditions for the bench mark case are given in table 4.1:

Table 4.1: Input parameters for the benchmark case

Property	Value
Foil thickness	10 μm
Film thickness	5 μm
Velocity	7.5 m/sec
viscosity	$0.8592 \cdot 10^{-3}$ Pa Sec
Young's Modulus	0.8 MPa
Number of nodes	160

Mesh convergence (see sec. 4.1) was checked before fixing the number of nodes to 160. In this section the pressure and load carrying capacity are normalized by using the normalizing scheme used by Hamrock [41]. In this the pressure is divided by the viscosity and velocity and then multiplied by length.

$$\mathbf{W} = \left[\frac{l.P}{(6.n.u)} \right] \quad (4.1)$$

Where

P = Average pressure

n = Viscosity

u = Velocity

l = Length of the modeling section

The same normalization scheme is used to make pressure dimensionless by replacing Average pressure with pressure acting on that particular node in Eq. (4.1). The normalization schemes for other variables are:

The film thickness is non-dimensionalized in the following way:

$$h^* = \left[\frac{h}{(r.l)} \right] \quad (4.2)$$

The foil thickness is normalized by length in the following way

$$g^* = \left[\frac{g}{(r.l)} \right] \quad (4.3)$$

Distance from the start of the modeling section or Cartesian coordinate x was made dimensionless by dividing with length and called as Position

$$X = \left[\frac{x}{l} \right] \quad (4.4)$$

4.1 Mesh Convergence

For any numerical simulation mesh refinement and mesh convergence plays an important role in increasing the accuracy of the results and optimizing the time taken to run the simulation. A mesh refinement was performed in this particular case starting with 80 nodes and ending with 400 nodes. Fig. 4.1 shows the resulting mesh convergence obtained when the number of nodes was varied. The plot was between dimensionless load and foil thickness ratio (see Eq (4.3)) with the number of nodes varying each time. From the plot and values it was observed that the load values for 160,240,320 and 400 nodes do not vary much. Many of the results differed by less than 1 % and the maximum variation in the results when the number of nodes was varied was found to be less than 10 %. So the number of nodes was taken to be 160 in order to save computational time while not compromising in accuracy of the results.

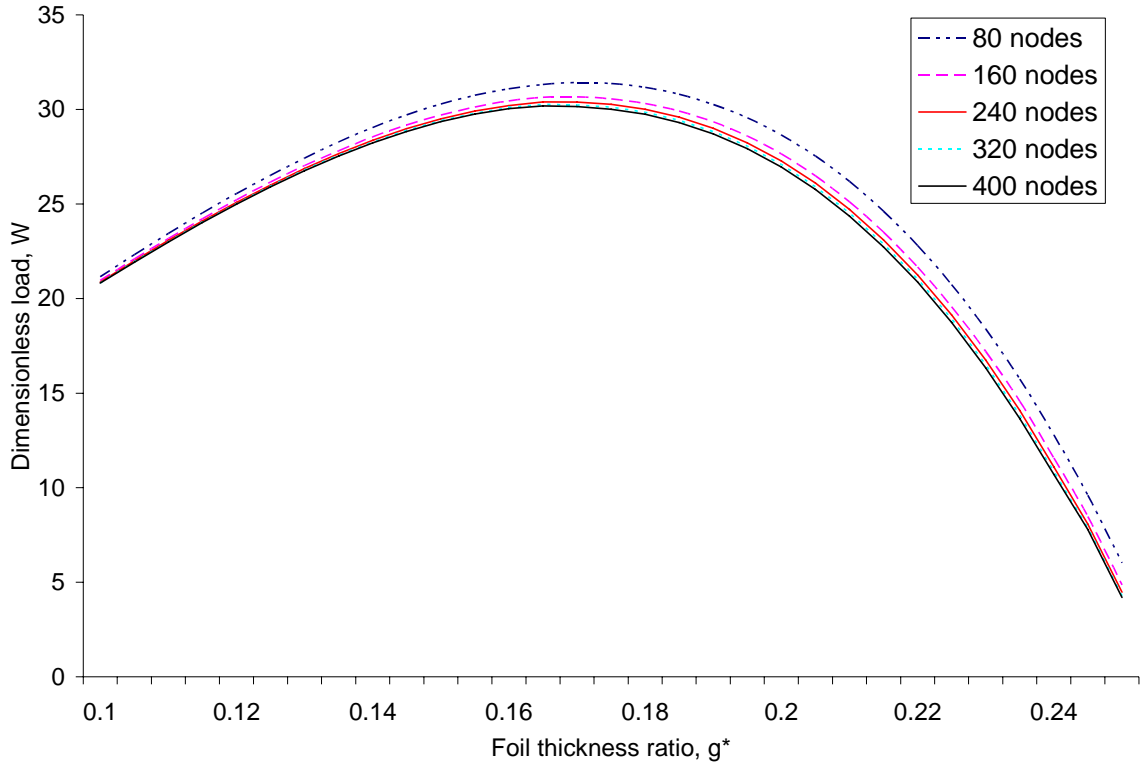


Figure 4.1: Plot showing the variation of dimensionless load used for mesh convergence

To test the uniqueness of the solution the initial conditions were varied in the model and the results were checked for any arising differences due to the presence of multiple solutions. The results remained same irrespective of the changes in the initial conditions which prove the uniqueness of the solution.

4.2 Pressure Profile

Figure 4.2 shows the variation of pressure over the entire length. Here the abscissa refers to the position which is distance from the end of the previous Microtexture divided by the length (see Eq. (4.4)). The pressure is nondimensionalised by dividing with the viscosity and velocity and then multiplying with the length (see Eq. (4.4)). This nondimensionalization scheme is used throughout this work to make pressure and load

carrying capacity dimensionless. Fig. 4.2 shows the variation of pressure over the surface for a film thickness of $5 \mu\text{m}$ and a foil thickness value of $10 \mu\text{m}$ (benchmark case). The pressure profile obtained is similar to that of the pressure profile generated in the sliding bearing case but differs at the peak in terms of the smoothness of the curve. In Fig. 4.2 the highest value of pressure occurs at the middle of the section whereas in the case of sliding bearing case the peak, depending on the shoulder height (s_h) occurs farther away from the middle of the section. The reason for the mentioned differences is that in the modeling section of the current work only the first half of the section deflects and so the geometry change occurs only for the initial half and the latter part is devoid of any profile changes. This is the reason for the sudden decrease of the pressure from the middle of the section to zero at the end.

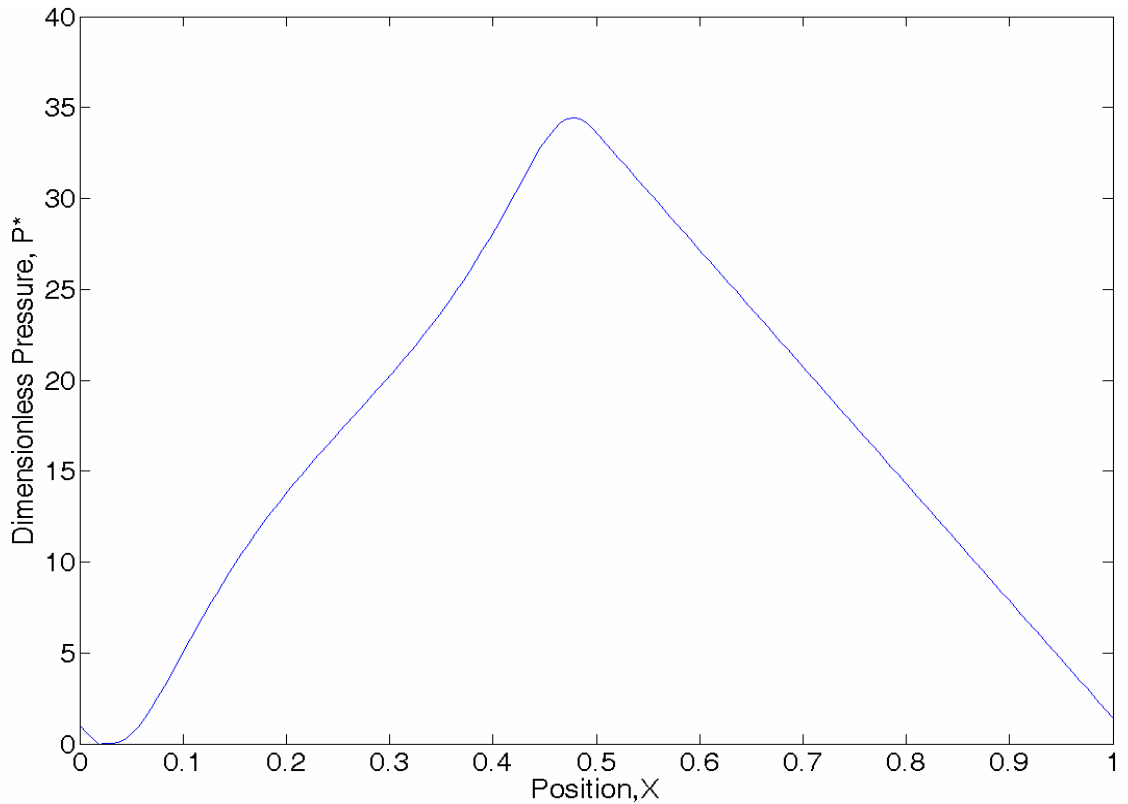


Figure 4.2: Plot of the Pressure profile over the section for the benchmark case

4.3 Pressure Profile for various film thicknesses

Figure 4.3 shows the pressure variation with respect to film thicknesses. The minimum film thickness is varied while keeping all other parameters constant. Fig 4.3 shows the pressure profiles for minimum or initial film thicknesses ranging from 3 μm to 9 μm . The amount of pressure exerted on the surface increases as the film thickness decreases. It can also be observed from Fig. 4.3 that varying the film thickness has effects on the shape of the pressure profile and as the film thickness increases the profile gets smoother. This may be due to the variations in the deflections. As the film thickness increases the uniformity in the deflections might be more pronounced which maybe the reason for the smoother pressure profiles.

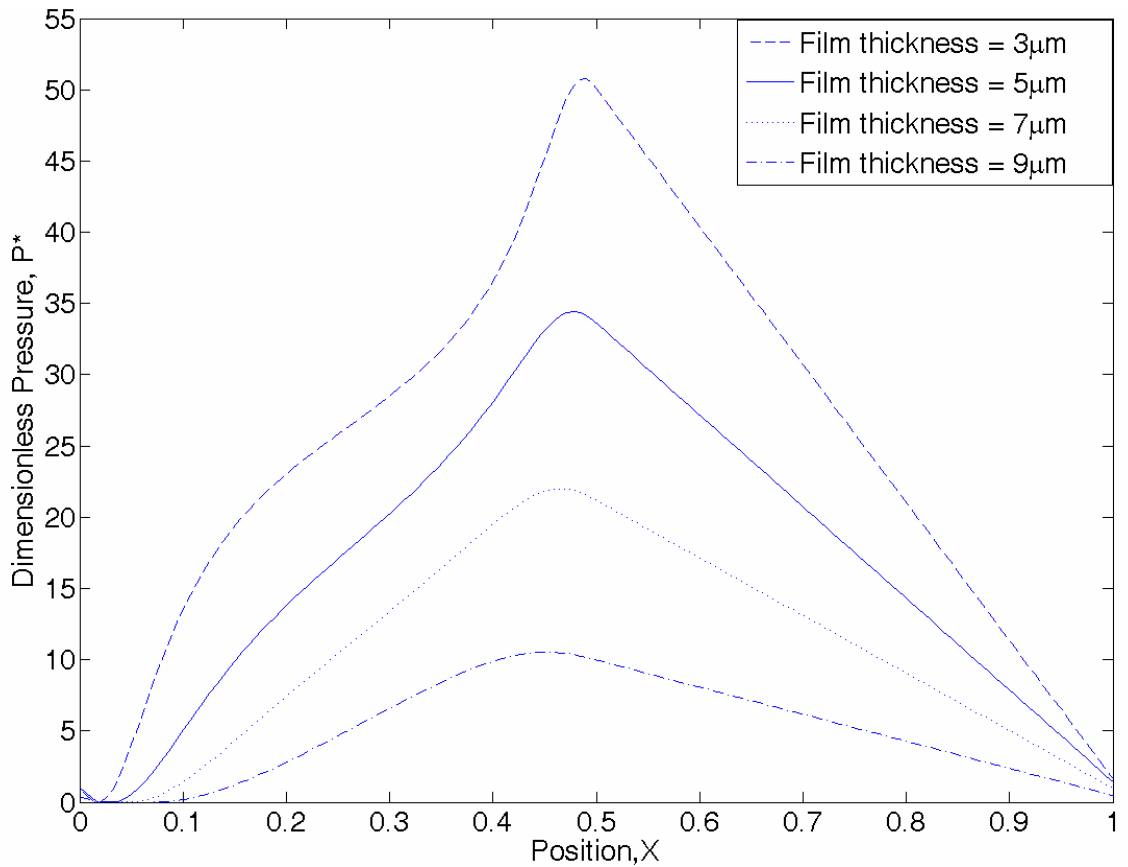


Figure 4.3: Plot of Pressure profiles for various film thicknesses

4.4 Pressure Profile for various foil thicknesses

Figure 4.4 shows the pressure variation with respect to foil thicknesses. The foil thickness is varied keeping all other parameters constant. The figure shows the pressure profiles for foil thicknesses ranging from 6 μm to 18 μm . In Fig. 4.4 the dimensionless pressure increases as the foil thickness increases, this trend continues up to a certain value and then the pressure or load starts decreasing. This value at which the maximum pressure or load support is generated can be termed as the optimum foil thickness value and can be used when fabricating the surfaces to improve the load carrying capacity. This is discussed in detail in section 4.13. Similar to Fig. 4.3 the pressure profiles are smoother at higher values of the foil thickness and again this may be attributed to the uniformity of the deformations of the surface at higher values of film thickness and foil thickness. The film thickness was maintained at a constant value of 5 μm (benchmark case) when generating the Fig. 4.4.

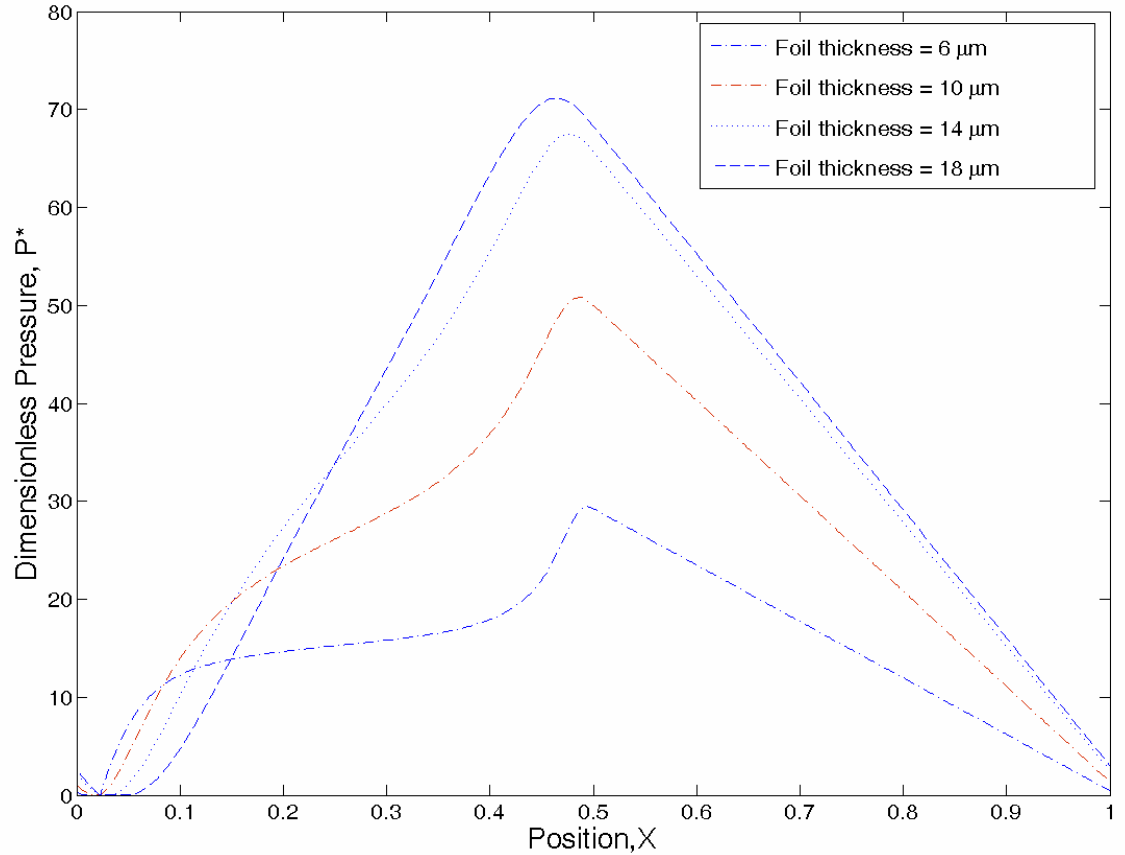


Figure 4.4: Plot of Pressure profiles for various foil thicknesses

4.5 Deflection profile for the bench mark case

The surface deforms due to the load being applied in the form of fluid pressure. The resulting deflection profile for the benchmark case is shown in Fig. 4.5. The deflection values for the second half of the surface are zero because the region is considered rigid and does not deform. The deflection is made dimensionless by dividing with the foil thickness of the textured surface (in this case the foil thickness is 10 μm).

$$D^* = \left[\frac{D}{g} \right] \quad (4.5)$$

The maximum deflection for the benchmark case (film thickness = 5 μm , velocity = 7.5 m/sec) is 18 μm .

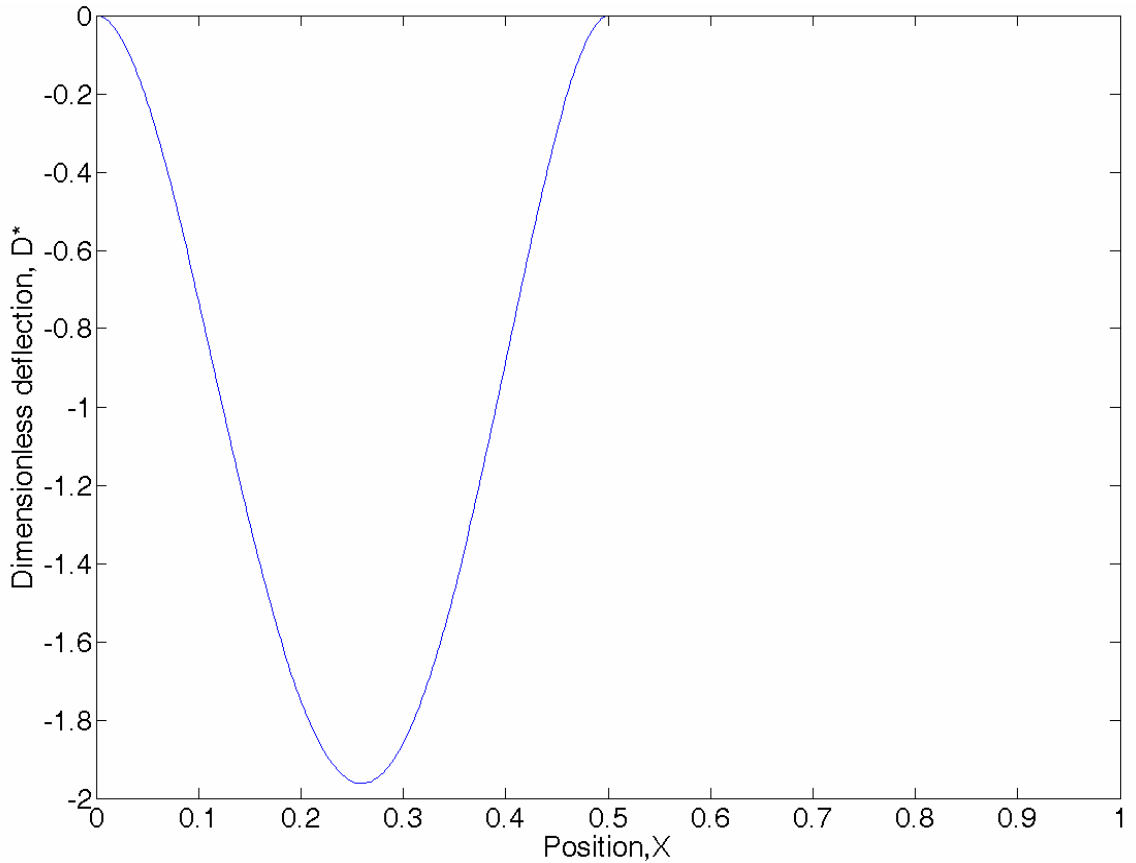


Figure 4.5: Deflection profile for the bench mark case of 5 microns

4.6 Deflection profiles for various film thicknesses

As the film thickness increases the amount of deflection decreases which means that the pressure or load applied decreases with the increase of film thickness. Fig. 4.6 shows the variation of deflection values for various film thicknesses. The values of all the variables like foil thickness, velocity and the ratio of deformable to undeformable regions (length ratio) are constant for all the above results. From Fig. 4.6 it can be observed that

the amount of maximum deflection is varying largely as we increase the film thickness. It is less than ten microns when the minimum film thickness is 9 microns and as the initial or minimum film thickness is decreasing from 9 to 3 microns the maximum deflection increases to 35 microns. It has been discussed in previous sections 4.3 and 4.4 about the effect of film thickness on pressure and load. The load decreases as the film thickness increases and so the deflections too decrease with increase of film thickness values.

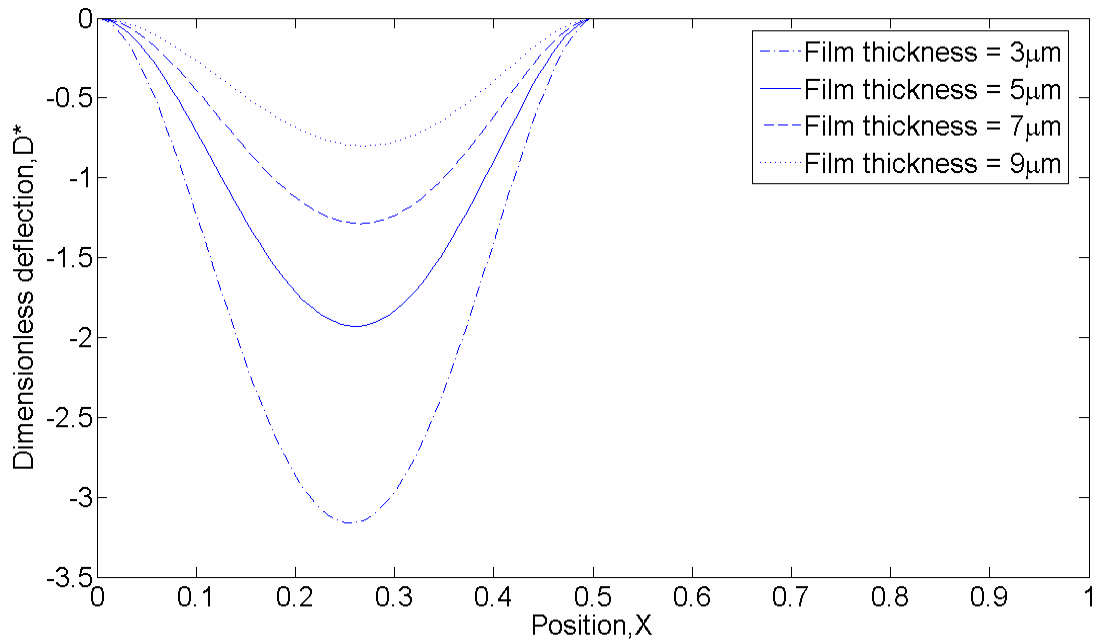


Figure 4.6: Variation of deflection with film thickness

4.7 Film Thickness Profile for the benchmark case

Figure 4.7 shows the profile of the film thickness along the surface. The film thickness is nondimensionalised by dividing with the deformable length as shown:

$$h^* = \left[\frac{h}{(r.l)} \right] \quad (4.6)$$

The maximum film thickness is the sum of the minimum or initial film thickness and the maximum deflection. The film thickness remains constant in the stiff region or undeformable region of the section. The film thickness profile is identical to the

deflection profile because, film thickness is the sum of initial or minimum film thickness and the deflection at that particular node. The plot is generated for the benchmark case of film thickness $5 \mu\text{m}$ and foil thickness of $10 \mu\text{m}$.

$$h(i) = h_0 + \delta(i) \quad (4.7)$$

Where

$h(i)$ = value of film thickness at i^{th} node

h_0 = minimum or initial film thickness in μm

$\delta(i)$ = value of deflection at i^{th} node

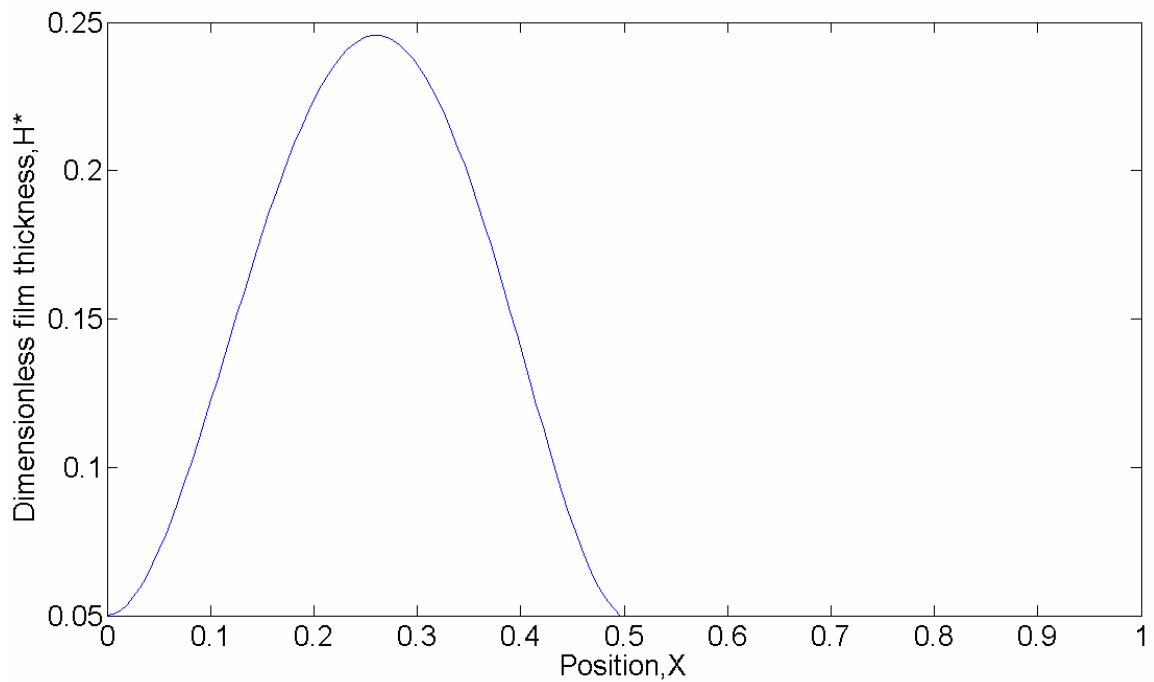


Figure 4.7: Variation of film thickness along the textured surface

4.8 Defining the yielding limit

The load or pressure acting on the surface should not exceed the yield strength of the material used to make the micro textured structure. If the stress is too high the thin layer or foil will yield and the surface will fail. Thus, a realistic prediction would take into consideration the yielding of the material and recommend only those combinations of minimum fluid film thickness and foil thickness which will not result in yielding. The yielding criterion used in this work was taken to be a very conservative one. By conservative it means that it was assumed that the surface is being acted upon by a point load where in reality the surface is acted upon by a distributed load. A point load produces a greater moment than a distributed load, so that the predicted stress is higher and this type of loading will give a very conservative prediction of the force which causes yielding. The above described method of calculating the yielding limit accounts for a greater factor of safety.

$$\sigma = \frac{M * Y}{I} \quad (4.8)$$

where σ = Tensile yield strength

The maximum moment occurs at the center of the beam where a point load is acting on a fixed-fixed beam. The moment M is:

$$M = \frac{P * L}{8}$$

Simplifying and rearranging the expression for load P , which is required to act on the structure in order to yield gives:

$$P = \frac{16\sigma I}{Lt} \quad (4.9)$$

Substituting for $I = \frac{bt^3}{12}$

$$\text{Therefore: } P = \frac{4\sigma bt^2}{3L} \quad (4.10)$$

Tensile strength of PDMS (from MIT website for material properties) is:

$$\sigma = 2.24 \text{ MPa (for PDMS)}$$

The load P when calculated came to 0.12 N.

This load when divided by area gives a critical pressure value which was plotted in Fig. 4.8 to mark the film thickness at which the surface yields. It has been made sure that the numerical simulations were performed with film thicknesses above the value that lead to yielding. The load at which yielding occurs is proportional to the squared foil thickness and inversely proportional to the length of the structure. This means that thicker foils can sustain greater loads before yielding. Figure 4.8 was generated for the benchmark case by keeping variables like foil thickness and velocity constant.

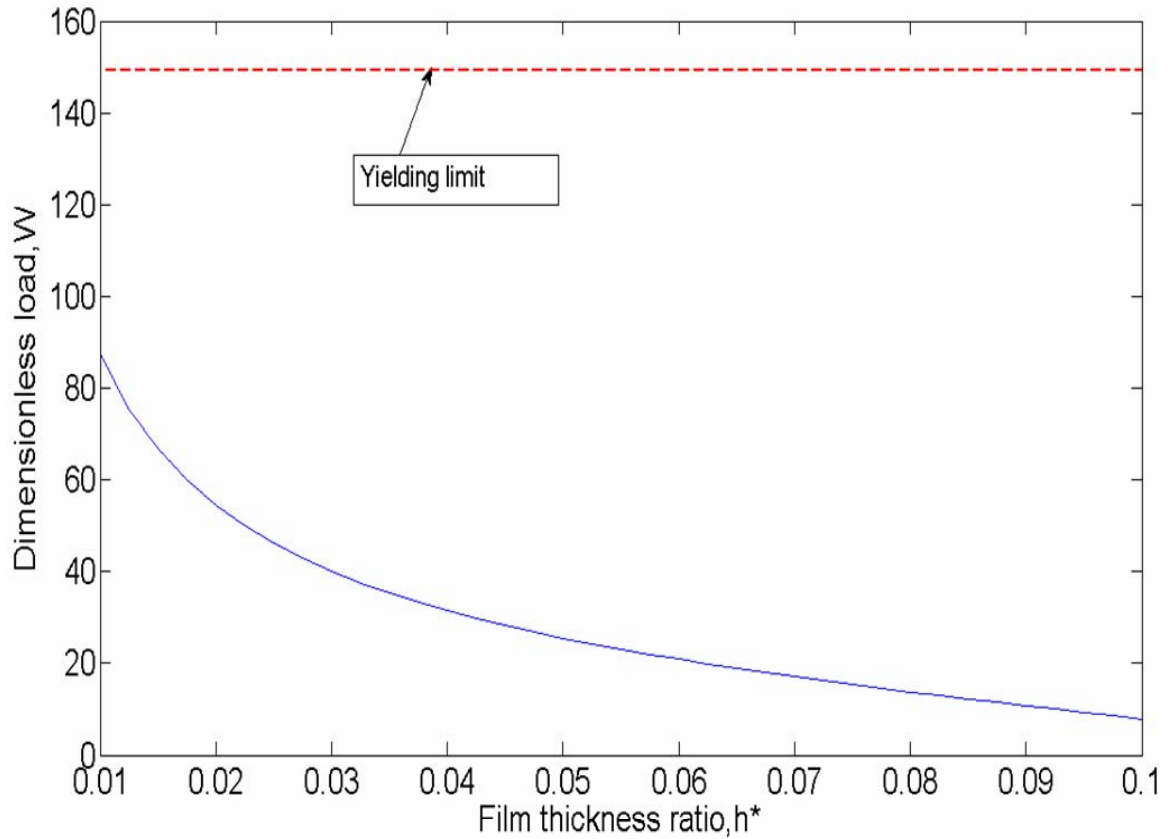


Figure 4.8: Variation of dimensionless load carrying capacity with film thickness

4.9 The effect of film thickness and velocity on Average pressure

Velocity plays an important role in generating the load support. Fig 4.9 displays the results of a parametric study by varying the velocities of the opposing surface to the PDMS specimen. All the velocities are realizable when performing the experiments with the experimental setup which will be discussed in later sections and are also similar to those expected in real applications. The plot gives a good indication to the effect of changing velocities on average pressure or load support. It is evident from the plot that as the velocity increases the Average pressure increases and so do the load support. The variation of the pressure follows a similar pattern for all the velocities. Note that the plot

is generated between two dimensional quantities of average pressure and film thickness. The reason for doing this is due to the nondimensionalizing scheme followed in which we divide with velocity to make load dimensionless as shown in Eq. (3.1).

In this section the velocity is not constant but varies for each case so a plot was made with dimensional variables to show the net effect of velocities on the pressure or load support. In Fig. 4.10 the normalizing scheme was employed and the plot was generated between the nondimensionalized quantities of load carrying capacity or dimensionless load and film thickness ratio which is film thickness divided by the deformable length.

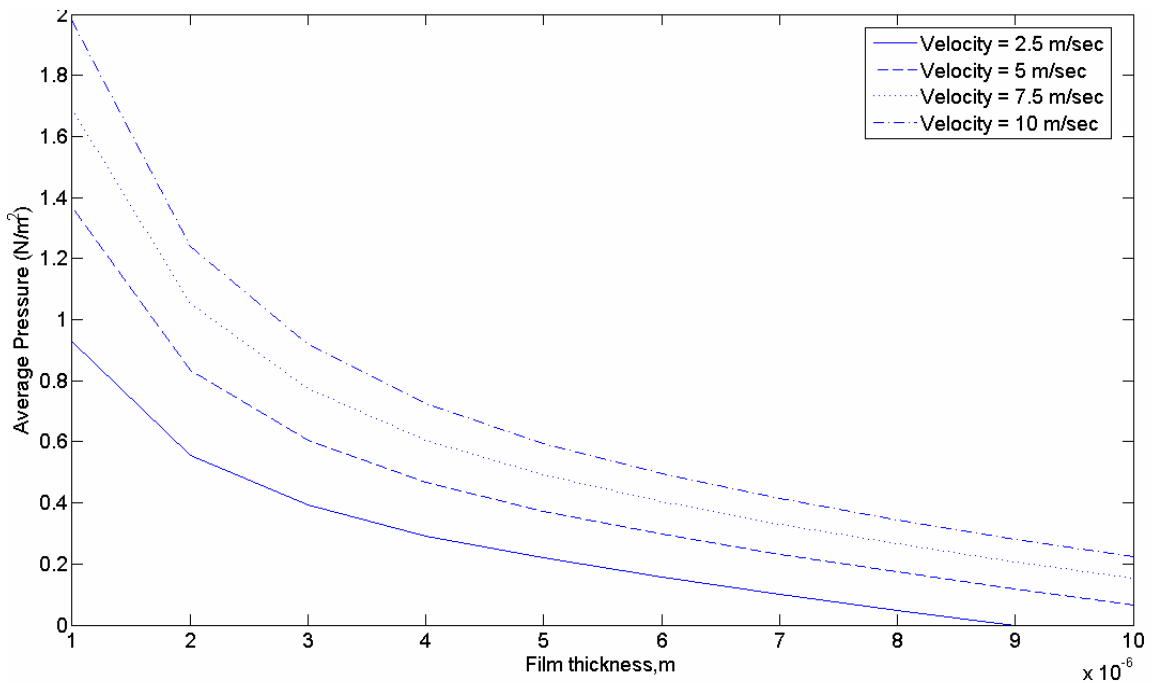


Figure 4.9: Plot of average pressure as a function of thickness for various velocities

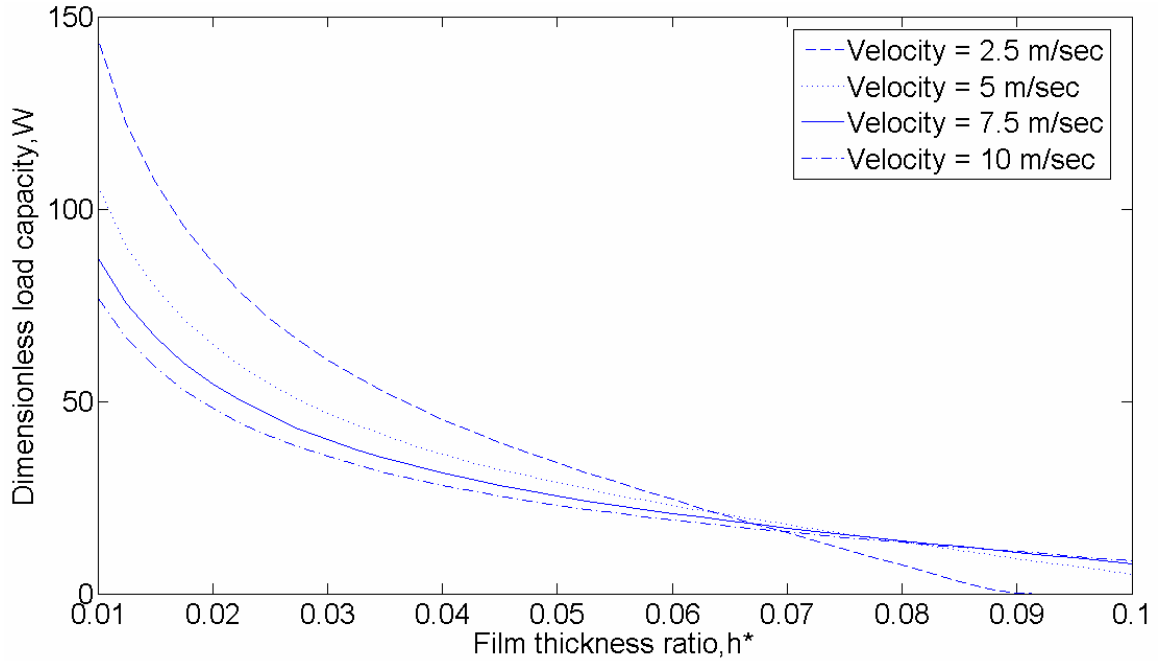


Figure 4.10: Plot of dimensionless load as a function of film thickness ratio for various velocities

In Fig. 4.10 in order to make the load dimensionless the pressure was divided by the corresponding velocity. In Fig. 4.10 due to the normalization scheme employed the results are different than Fig. 4.9 and collapse into one another to show that the dimensionalization scheme works well.

4.10 The effect of film thickness ratio and foil thickness on dimensionless load capacity.

The above plot is the one done for various foil thicknesses. As the foil thickness increases the load support increases to a certain extent and decreases thereafter due to the decrease in flexural rigidity. An effort will be made to find the optimum foil thickness

which gives maximum load support without any chance of yielding of which you will read in later sections (sections 4.13, 14, 15).

In Fig. 4.11 the foil thickness values used are 10 15 and 20 μm . The yielding limit for the foil thickness of 10 μm is also shown to give an idea about the magnitude of the dimensionless load capacity when compared to yielding limit. As the yielding limit is directly proportional to the square of the foil thickness, the yielding limits for the cases of 15 and 20 μm are too high to be included in the chart. So, as the foil thickness increase in value the yielding limit also increases by a power of 2. In other words if the foil thickness is high the foil will yield at a higher value of film thickness which might suit to some situations where very low film thicknesses are required.

In Fig. 4.11 the curves also start to change over the range of film thickness ratios. The trends reverse after a certain value of film thickness ratio; initially the largest foil thickness value produces highest load capacity and as the film thickness ratio increases the trend reverses and at a film thickness ratio of 0.07 the smallest foil thickness produces the highest load than the other two. Also note that at higher film thicknesses the load carrying capacities of the higher foil thicknesses tend to zero.

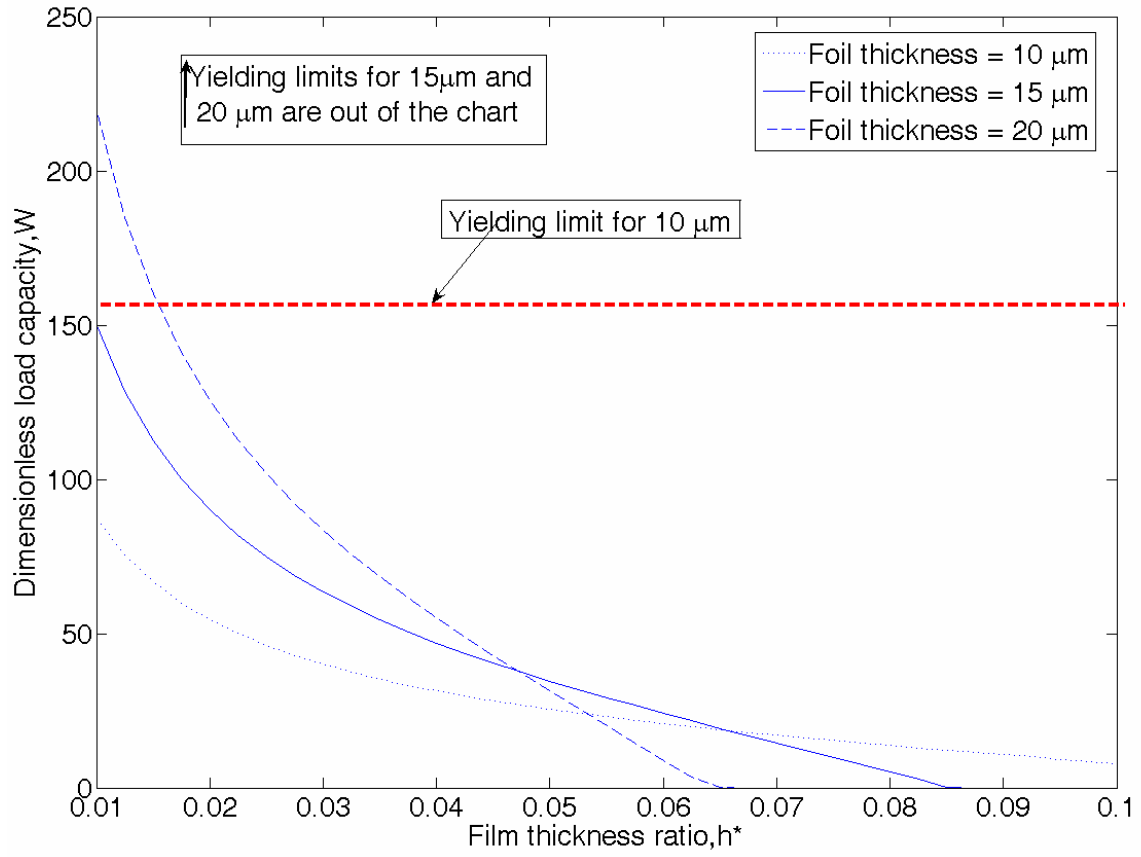


Figure 4.11: Figure with dimensionless load variation for various foil thicknesses

4.11 Static vs. deformable case

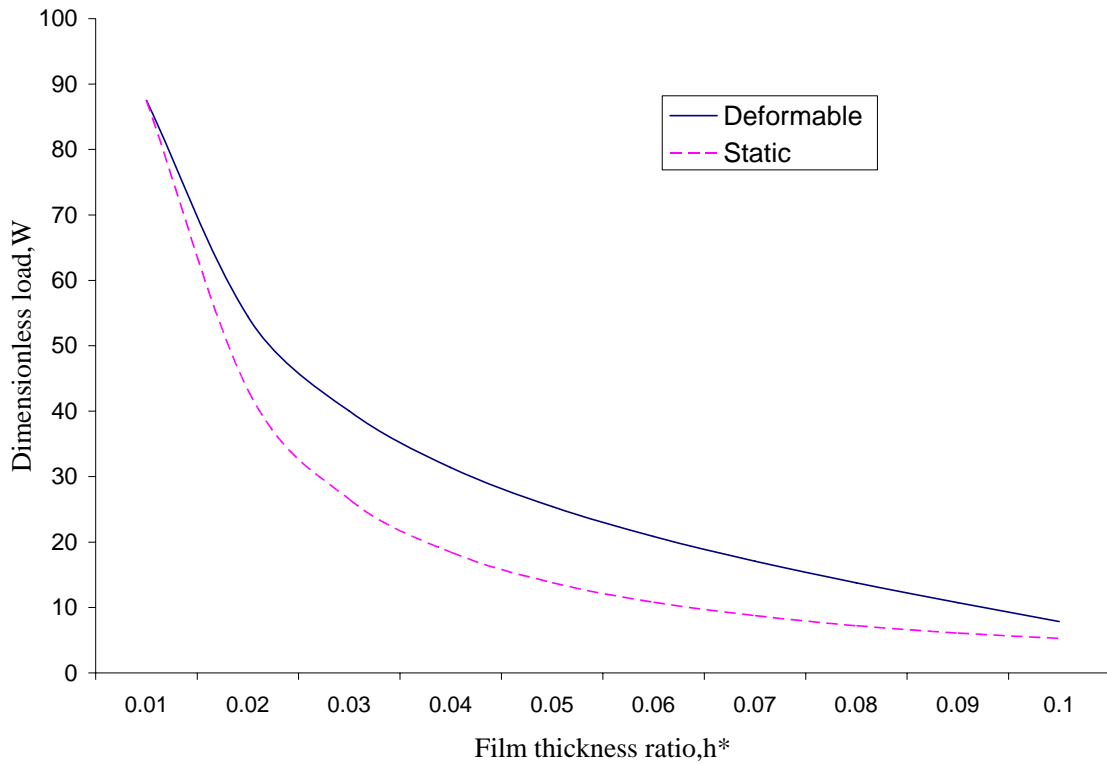


Figure 4.12: Comparison of the deformable surface with the non deformable

The static or non deformable surface was simulated in the following fashion. The static surface was assumed to have a geometry which is identical to the geometry of the deformable surface at a particular initial film thickness value, but there will be no change of geometry in the static surface due to fluid pressure whereas in the case of a deformable surface the change of geometry occurs. For this particular case the static case was assumed to have the same geometry which is similar to the deformable surface at an initial or minimum film thickness value of $1 \mu\text{m}$. This was incorporated in the numerical model by taking into account of the deflection values for a deformable geometry and

neglecting the same for a static case. The load carrying capacity was determined by solving numerical form of Reynolds equation alone for static surface.

Figure 4.12 shows the variation of load for both deformable and non deformable surfaces. This is an important plot with regard to the advantages possessed by the deformable or adapting surfaces as it shows that the surfaces adapt themselves while deforming and there by resulting in higher load carrying capacity. In this plot (fig 4.12) the film thickness is varied from 1 to 10 microns.

4.12 Comparison of film stiffness for deformable and static cases:

It has been mentioned in previous sections that the adapting surfaces generate more load support than non adapting surfaces because of the increase in the fluid film stiffness. In this section the film stiffness of both the deformable and static surfaces is compared (see Fig. 4.13). The non dimensional film stiffness is plotted against dimensionless film thickness for the static and deformable cases and the results show that the fluid film stiffness of the deformable is more than the stiffness of the static for majority of the dimensionless film thickness. By adjusting the parameters or input conditions of the numerical model it can be shown that the deformable fluid film stiffness is greater than stiffness for the static case for the entire dimensionless film thickness.

In Fig. 4.13 although the stiffness of the static surface is greater than the deformable surface initially, as the film thickness increases the fluid stiffness of the deformable increases and surpasses the static case and continue to remain higher than the static case. When the film thickness is around 10 μm the film stiffness of the deformable is almost 300 % more than the stiffness of the static surface. This shows that the

performance in terms of load carrying capacity is better for deformable surface than the static surface.

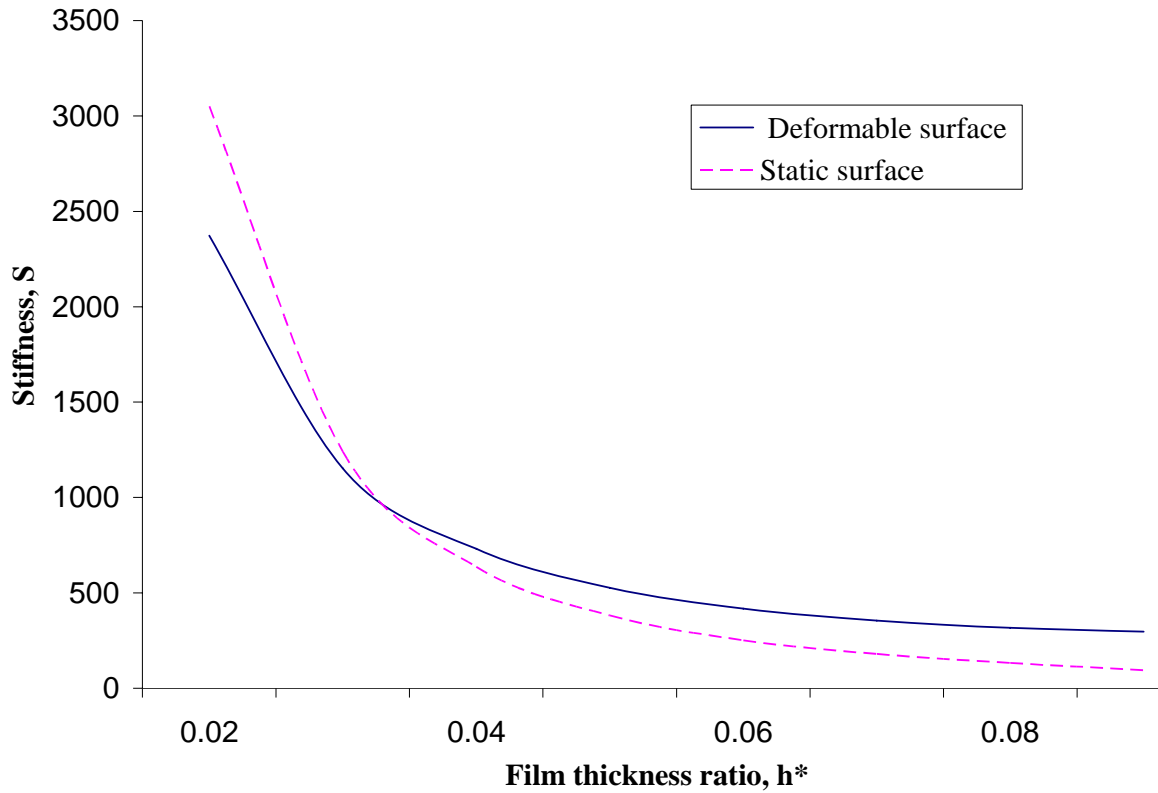


Figure 4.13: Plot of Non dimensional film stiffness and dimensionless film thickness

4.13 Variation of load with foil thickness value, g^*

When the value of foil thickness is increased, the load carrying capacity increases initially and after a certain value it decreases. This shows that there is an optimum value of foil thickness at which the largest load carrying capacity is generated for a particular film thickness value. Fig. 4.14 is the plot of variation of load carrying capacity with the foil thickness value. In the figure load carrying capacity is increasing up to a certain value and decreases thereafter. This can be described as the optimum foil thickness value for

the particular film thickness considered. In this plot the film thickness value was taken as the benchmark value of $5\ \mu\text{m}$. determining an optimum geometry makes the surface more effective by generating a higher value of load carrying capacity than for an arbitrarily chosen foil thickness value.

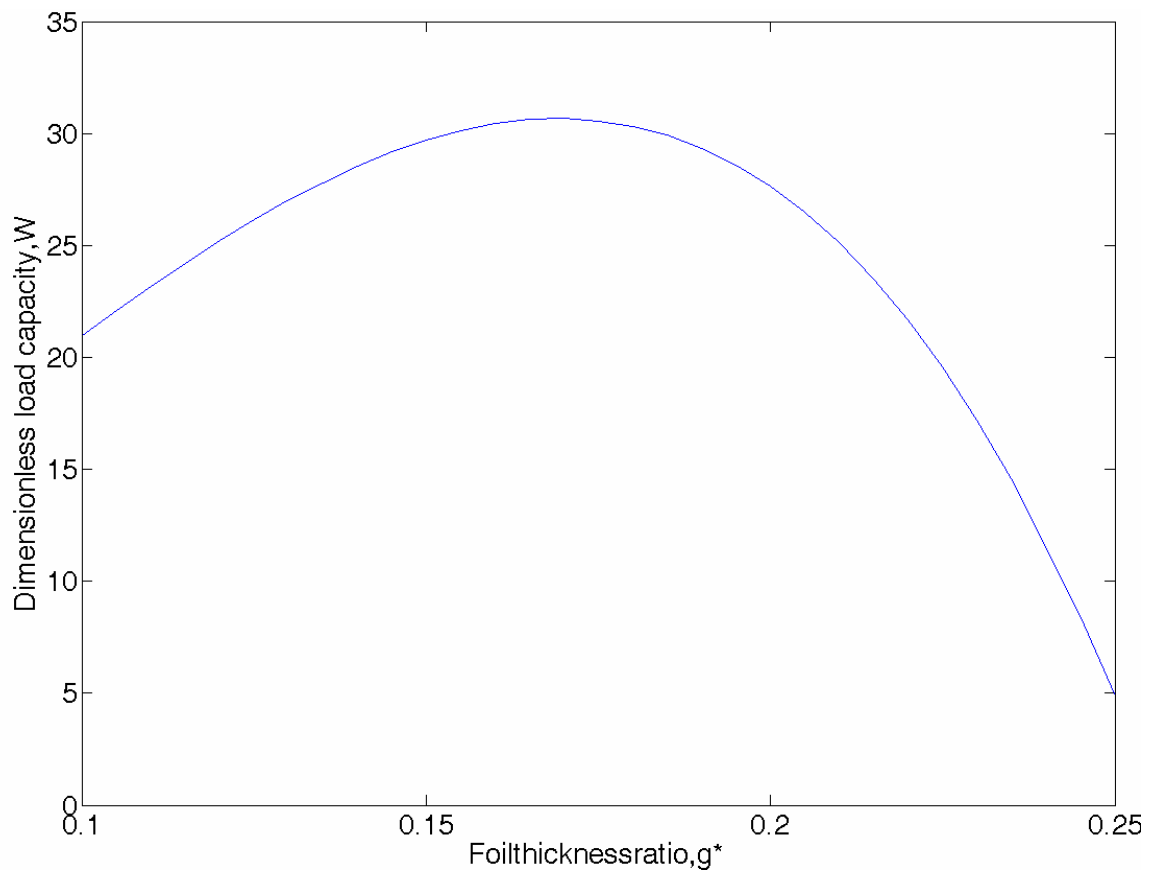


Figure 4.14: Variation of dimensionless load with foil thickness ratio for the benchmark case of $5\ \mu\text{m}$

4.14 Variation of load with foil thickness for a film thickness value of 3 μm :

Figure 4.15 contains a plot of the dimensionless load (W) as a function of the foil thickness ratio (T). When compared to Fig 4.14 the present plot spans over a large range of foil thicknesses due to the low film thickness value. The optimum foil thickness value for a minimum film thickness value of 5 μm is approximately 19 μm whereas the optimum foil thickness value for a film thickness of 3 μm is 28 μm . This shows that as the value of film thickness decreases the optimum geometry results in higher values of foil thickness.

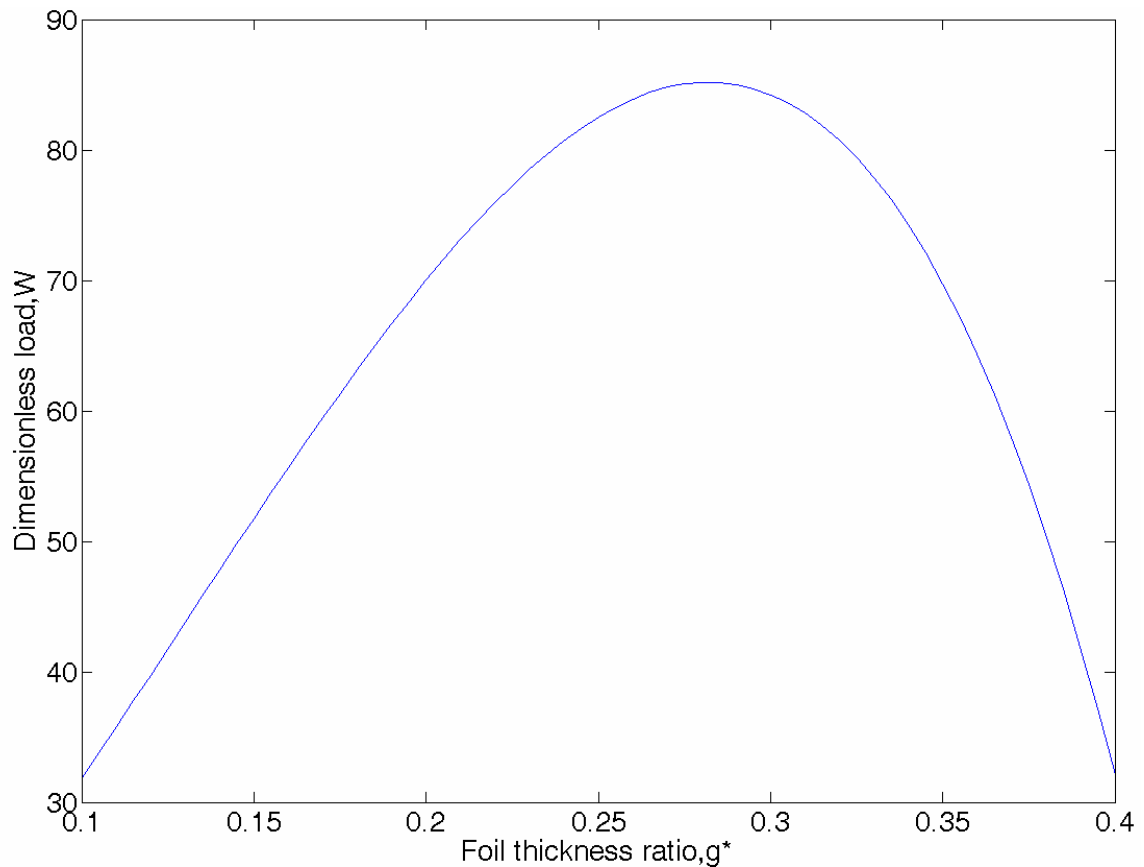


Figure 4.15: Variation of dimensionless load with foil thickness for a film thickness of 3 μm .

4.15 Variation of load with foil thickness for a film thickness value of 7 μm :

Figure 4.13 displays to the plot between dimensionless load and foil thickness ratio for a minimum film thickness value of 7 μm . It is evident from the plot that as the minimum film thickness value increases; the optimum geometry corresponds to a lower value of foil thickness. The optimum foil thickness for a minimum film thickness value of 5 μm is approximately 19 μm whereas for a film thickness value of 7 μm , the value is approximately 12.5 μm . The plot of the optimum foil thicknesses at which maximum load support is generated for various minimum or initial film thicknesses is shown in Fig. 4.17. To summarize, smaller the film thickness values higher the foil thickness value corresponding to the optimum geometry and vice versa.

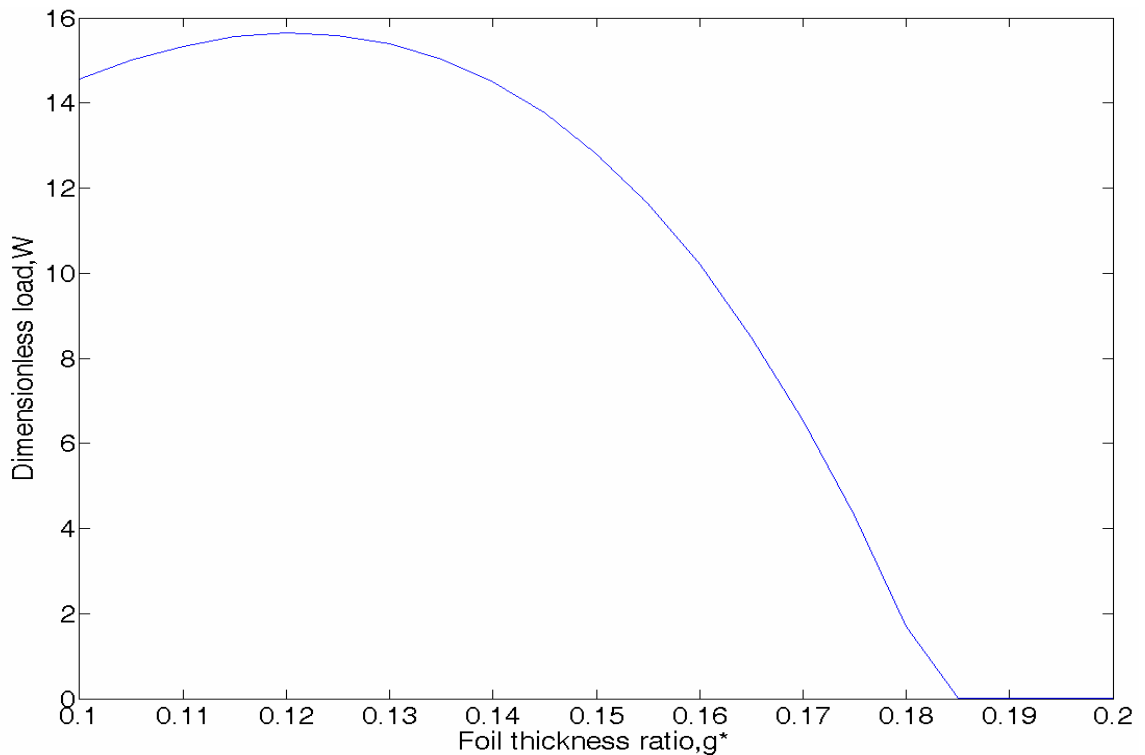


Figure 4.16: Plot of dimensionless load and foil thickness for film thickness of 7 μm .

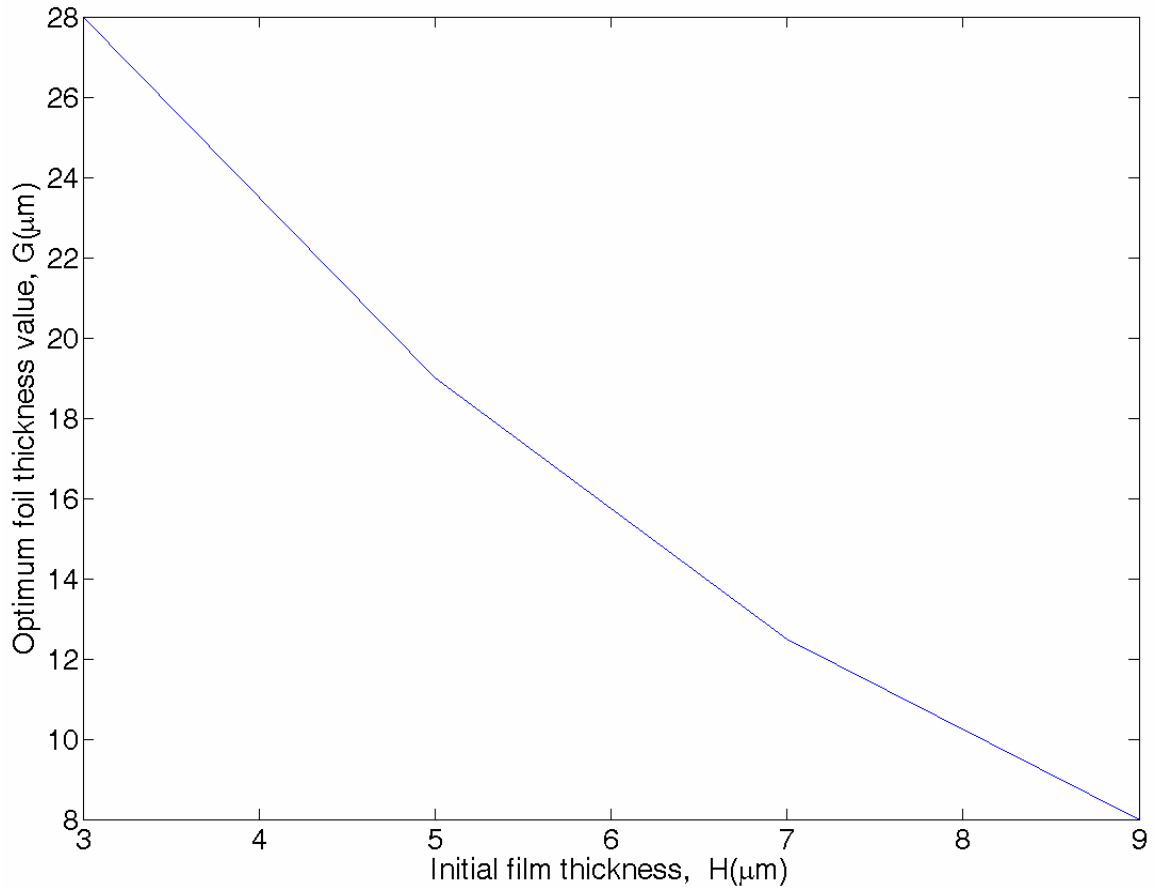


Figure 4.17: Plot of optimum foil thickness for various initial film thicknesses.

4.16 Plot of Dimensionless load for various length ratios:

As mentioned previously in this work, in the modeling section the deformable region and the stiff region are equal in length. The length ratio is defined as the ratio of length of deformable region to the total length which is 0.5 for the standard or benchmark case. In this plot the length ratio is varied from 0.25 to 0.75. Effectively the length of the deformable region is either decreased or increased to see the effect it has on the load carrying capacity. The length ratio of 0.25 was expected to yield low dimensionless load capacity values as the length of the deformable region is decreased but surprisingly it yielded high values initially and then the load carrying capacity went to zero. The zero

load carrying capacity might be due to the failure to produce any significant deflection at high film thickness values. The length ratio of 0.75 in which the length of the deformable region is increased, produced high values of dimensionless load carrying capacity but the difference between the length ratio of 0.5 and 0.75 decreased with increased high film thickness values. This shows that if a length ratio of 0.75 is employed at lower film thickness values higher load carrying capacities can be generated. The film thickness ratio in this plot is nondimensionalised by dividing with the total length unlike other cases where it was divided by the deformable length. This was done to have a uniform abscissa for all the cases. Although geometries can be altered easily in numerical modeling the same cannot be said in experimental testing. Fabrication of certain type of geometries might prove to be difficult.

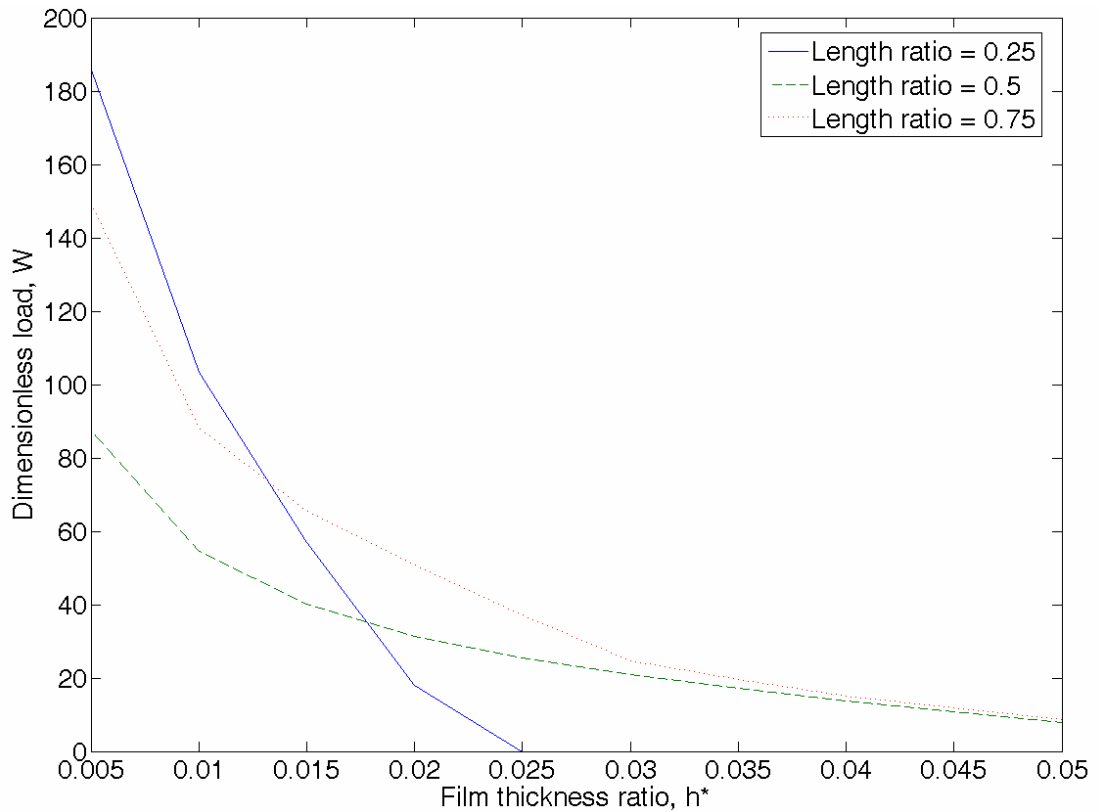


Figure 4.18: Plot of Dimensionless load for various length ratios.

CHAPTER 5

EXPERIMENTAL METHODOLOGY

As mentioned earlier the purpose of the numerical modeling was to give an insight of what to expect in experimental testing and ways to improvise the performance by optimizing the parameters before the fabrication of the surfaces. It has been proved theoretically that the adapting surfaces perform better than the static surfaces. The proposed self- adapting structures need to be tested experimentally under real time operating conditions to establish their better performance. For experimental purposes the self- adapting or smart surfaces were fabricated using micro fabrication techniques which will be discussed in detail in the following sections. The surfaces were fabricated with Polydimethylsiloxane (PDMS), a polymer known for its ease of design and fabrication. A test rig was designed and built to test the surfaces in real operating conditions of velocity and load. Details about the design of the test rig will be discussed in the following sections. However due to the paucity of time experiments could not be conducted in the course of this work and were deemed as the future scope of the work.

5.1 Surface Micro-Fabrication

The surfaces will be fabricated using proven micro fabrication techniques called ‘multilayer soft lithography’ [44], so that reliable prototypes will be produced that can be quickly tested for proof of concept and then applied to real applications. The micro fabrication technique is outlined in Fig 5.1

The first step is the chip designing with CAD programs. The next step is the fabrication of microstructures on silicon wafers with conventional photolithography. Then, based on the microstructures, surface micro fabricated devices are made out of transparent silicone polymer such as Polydimethylsiloxane (PDMS).

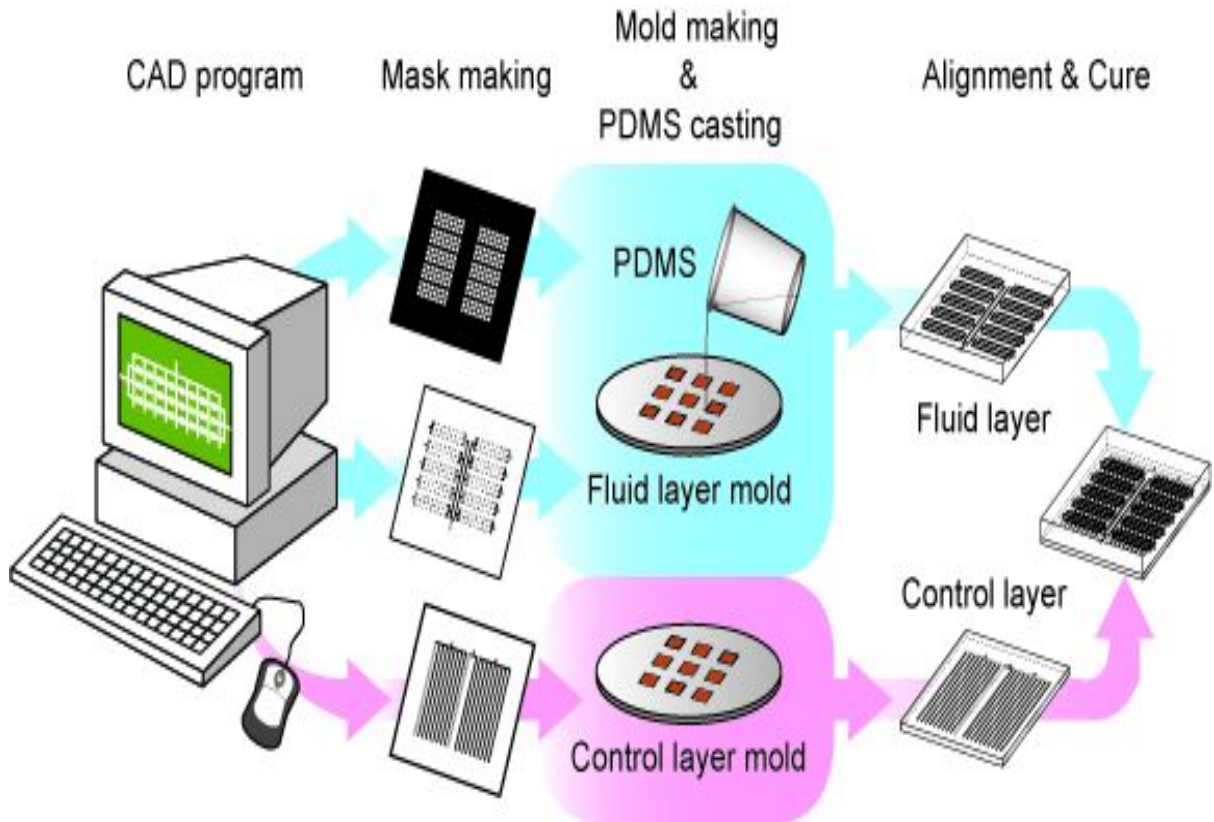


Figure 5.1: Schematic flows of the surface micro fabrication with multilayer soft lithography.

5.2 PDMS chip preparation process

The chip preparation is started by the preparation of the mold which then is used to prepare the specimen. Next a thin layer of PDMS is spin coated and bonded to the specimen resulting in the designed geometry for the surface. The entire process is done in

a clean room environment and the process usually takes an entire day. The mold was fabricated at the Alabama Microelectronics Science and Technology Center (AMSTC), located at and run by Auburn University.

5.2.1 Preparation of mold:

The silicon wafer needs be cleaned using the RCA cleaning process. This is done to make the wafer turn hydrophobic from hydrophilic which also helps in removing the oxide layer on the wafers. The second step is to apply the photoresist (SU-8) by the process of spin coating. The thickness of the photoresist is dependent on the acceleration, speed and time of the process. After ensuring the uniform layer of photoresist, we proceed to soft baking. We do it in two ways i.e. two minutes at 65⁰ F and 5 minutes at 95⁰ F. The next step is exposure of the wafer to the mask. This is an important task because the depth of the mold is dependent on the power, the intensity of the light source and the time of exposure. This is followed by hard baking for two minutes at 65⁰ F and eight minutes at 95⁰ F. This is the time when the mold on the photoresist hardens. Now we need to remove the rest of the photoresist, this process is called developing. In this process the SU-8 developer is poured into a dish and the wafer is dipped into it for approximately a minute and then taken out and treated with propanol. If there is any white jelly like appearance on the wafer that shows that it is not fully developed and so it needs to be dipped in the developer again. A fully developed wafer is the mold which can be used to make the PDMS chip.

5.2.2 Preparation of the PDMS specimen:

Prepolymer A and curing agent B need to be mixed in the ratio of 10:1 to make PDMS (Polydimethylsiloxane). The mixture needs to be vacuumed roughly for 2 hours to get rid of the air bubbles present in the mixture. After making sure that no air bubbles are present in the mixture, it is poured into an enclosure containing the mold and baked at a temperature of 80⁰ F for 45 minutes. After this the chip is peeled off from the mold. The surface is treated with CTMS (chlorotrimethylsilane) before this process to enable easy peeling off, resulting in less damage of the mold.

A blank clean silicon wafer is taken and is treated with CTMS. Treating with CTMS is required for the silicon wafer because it facilitates peeling off. If the wafer is not treated adequately, the mold may get damaged when the structure is being peeled off. Spin coating is performed with PDMS on this wafer. The thickness of the PDMS on the wafer depends on the velocity and the time of spin coating. The PDMS for this process is prepared with the mixing of components in the ratio of 20:1 (10:1 for chip preparation). This wafer with the thin layer of PDMS is placed in the oven for 30 minutes at a temperature of 80 F. after taking the wafer out of the oven the chip is turned upside down and placed on the thin layered wafer. The entire piece is again placed in the oven for a period of one hour to facilitate good bonding of the thin layer to the chip. The entire chip is cut off from the wafer. This marks the completion of the process of preparing a PDMS prototype specimen.

5.3 Mold making protocol

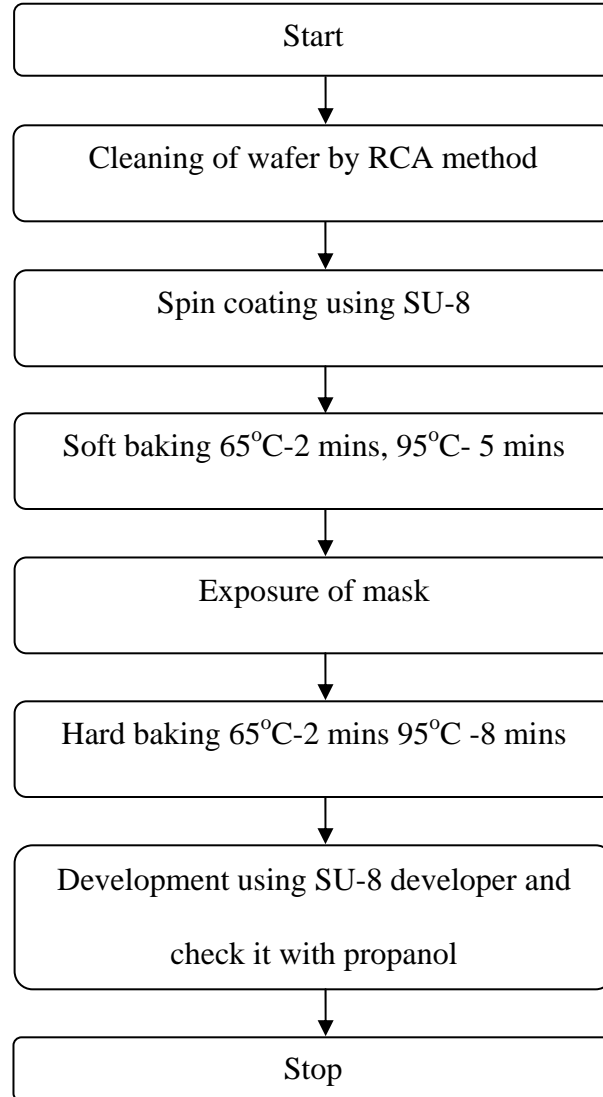


Figure 5.2: Figure describing the steps in the preparation of Mold surface

Photograph of the mold:

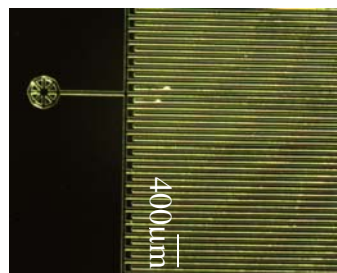


Figure 5.3: Microscopic view of the mold

5.4 Chip Preparation Protocol

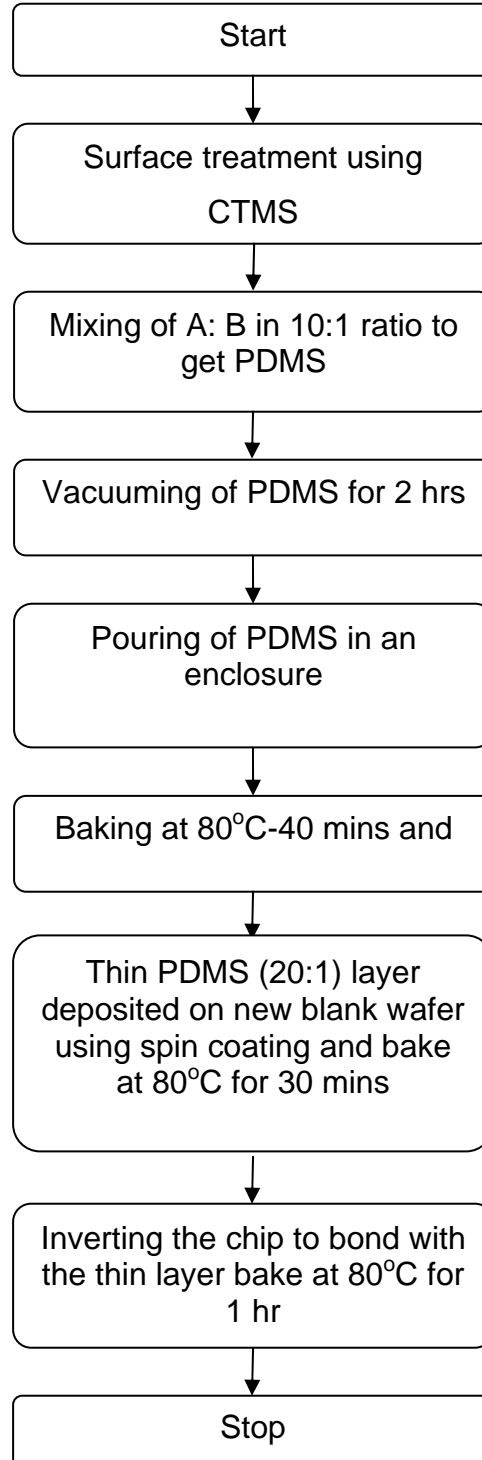


Figure 5.4: Figure describing the steps in the preparation of PDMS surface

5.5 Experimental setup

The experimental setup is as shown in the Fig. 5.5. The two contacting surfaces are a hard disk platter (selected for its smoothness) and the PDMS (Polydimethylsiloxane) self-adapting surface sample. The lubricant used is water. The moving surface (hard disk platter) is powered by a brushless DC motor whose power output was 1/8 Hp (90 Watts). The speed was observed through a motor speed indicator which comes as an accessory to the motor. To precisely control the PDMS specimen, a combination of a linear ball bearing stage and a tilt platform is used. A load cell is used to determine the load acting on the surface which is connected to a computer using a modular signal conditioner unit (National Instruments). The experimental setup was designed to be small and compact so that the whole process of sliding can be observed through a microscope located above the surfaces which would give a clear picture of the process and film thickness.

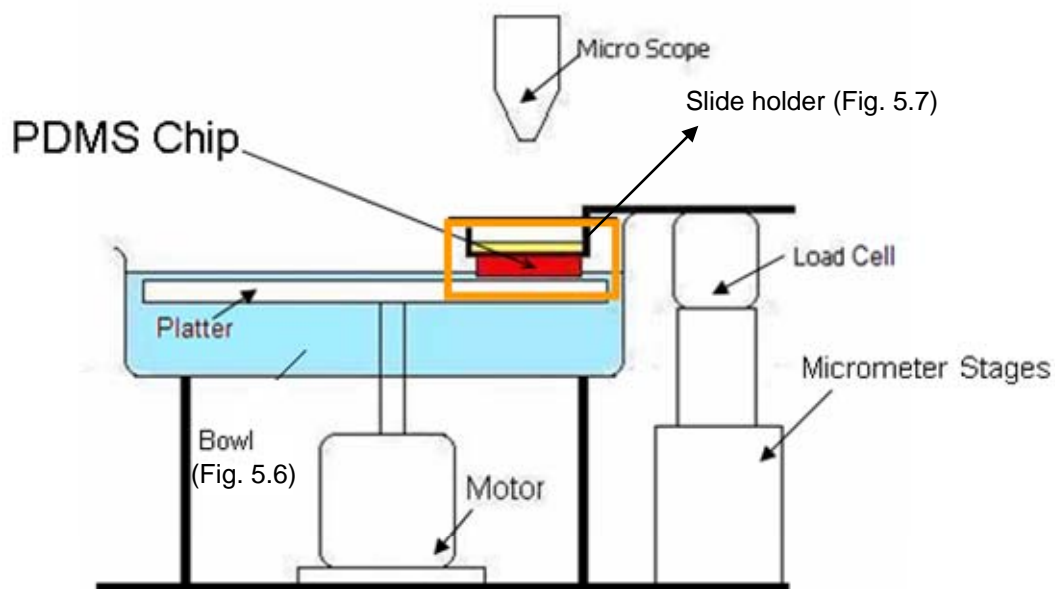


Figure 5.5: Experimental setup diagram showing various components used.

As mentioned above, the experimental setup is designed to be accessible so that the entire process could be monitored through the microscope for a good view and a better assessment. The view allows the user to ascertain the changes the surface undergoes while under pressure exerted by the fluid. The entire setup is situated on a base plate on which all the components are fastened securely. The motor is mounted vertically and is fastened to the base plate as shown in the Fig. 5.5. One of the limitations encountered during the design of the experimental setup was the space requirement because of the limited availability of space under the microscope in terms of width and height. So it was made sure that the motor chosen was of small size yet meeting the power and speed requirements needed for the experiments. The speed range of the motor is 0-2000 rpm and the area of the motor is 3.54 square inch. The shaft of the motor is projected into the bowl which houses the connecting part, from the motor to the hard disk platter which is used as the opposing surface. A suitable bearing was selected which could act as a connecting medium between the bowl and the motor. The bearing chosen was a ball bearing with an inner diameter of 12 mm and outer diameter of 32 mm. The inner ring of the bearing is glued to the shaft and the outer ring is glued to the bowl so as to allow the rotation of the shaft with the bearing. The bearing needs to be tightly sealed against any leakage of water which is filled in the bowl. The bearing was double sealed in order to ensure no leakage would occur. The bowl which is made of aluminum was also designed to fit with the motor and also ensuring enough space for the entire setup which includes the hard disk and the PDMS specimen. (See Fig. in the following page)

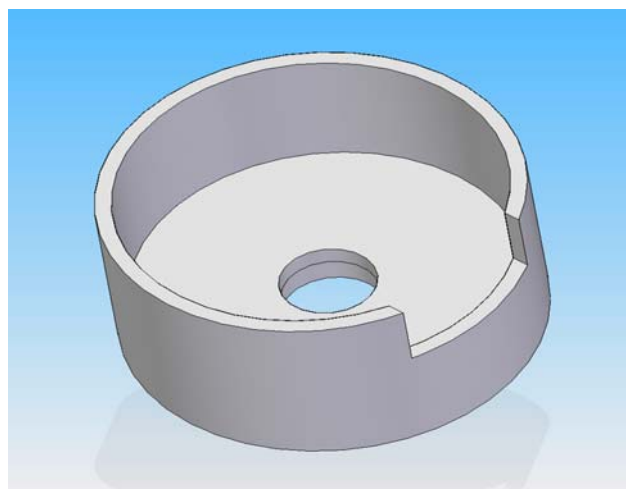


Figure 5.6: Design view of the bowl which houses the two surfaces to be tested

The bowl also was supported by support rods which were threaded into the base plate from the four sides of the bowl. This allows for the height to be adjusted. The shaft of the motor is connected to the disc with the help of a hub which was designed to facilitate the connecting of the motor shaft to the hard disk platter which are of different diameters. The adapting piece between the motor shaft and the hard disk platter is also made of aluminum with a high tolerance of 0.001 inch. The piece was designed to be perfectly in center with the shaft thereby limiting any vibrations which may result due to off centering of the adapting piece. The top of the adapting piece was designed as a projecting hub with the same diameter of the hard disk platter so that the platter would directly fit on top of the piece. A part was designed to hold down the platter and prevent it from moving away by drilling a screw through the piece.

It is important that the position of the specimen and disk can be adjusted so that they can be brought into close proximity while remaining nearly parallel. The PDMS chip

or specimen is glued to a glass slide to make it easier to hold and so a glass slide holder was designed which had projecting arms to which the glass slide could be tightened with the help of screws. The other end of the slide holder rests on the load cell as shown in the Fig 5.5. The main idea behind the design is to ensure that the load acting on the load cell should consist of only the fluid pressure exerted on the grooves of the PDMS specimen. For this purpose, one of the ends of the load cell was threaded into the slide holder so that the only load experienced by the load cell would be that of the fluid pressure on the grooves.

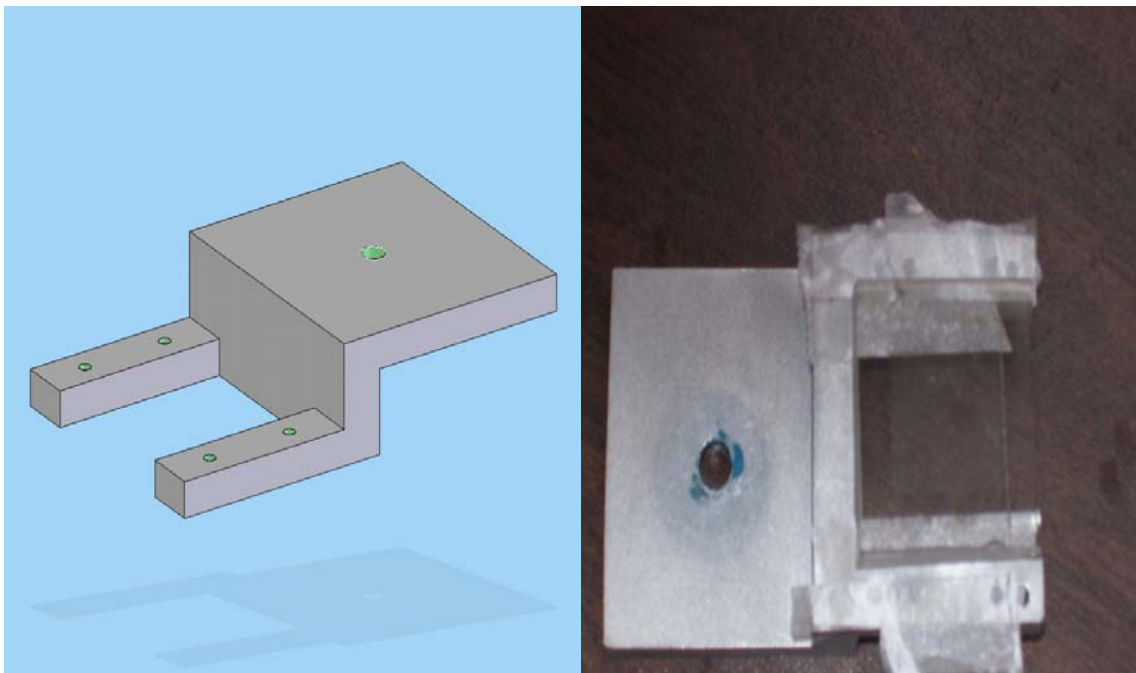


Figure 5.7: Design and photographic view of the slide holder which holds the PDMS specimen

The load cell is threaded on the other end to a height adjuster which is used to adjust height variations so that the PDMS specimen is at the same height as that of the

disk platter. The height adjuster is also made of aluminum and its basic purpose is to help in height adjustments so that the two opposing surfaces (platter and PDMS specimen) would be made to come in contact. The height adjuster is connected to the micrometer stage and has an adjustable slot through which the height of the slide holder can be controlled relative to the base plate. This would be especially useful to control the precise placement of the PDMS specimen in the bowl.

The micrometer stage used was a 25 mm aluminum ball bearing stage with a micro meter sensitivity of 10 μm and a minimum increment of 3 μm . Its main purpose is to allow precise control of the PDMS specimen and to help in ensuring that the opposing surfaces are parallel to each other. The height at the macro level can be taken care of by the height adjuster but when adjustments need to be made at a micron level we need a micrometer stage which aids in doing the job.

The micrometer stage has the advantages of occupying less space yet allowing movement precisely so as to make the two opposing surfaces parallel. It can also be put to use when we want to control the film thickness between the surfaces in microns. This can be done by first bringing the surfaces to contact and then raising the PDMS specimen for a few microns or to the height of the pre-determined minimum or initial film thickness. The micrometer stage offers movement in all the three (XYZ) degrees. The stage is threaded to the base plate.

5.6 Experimental Scheme

The experimental scheme involves bringing the surface to contact and then raising the PDMS to a certain pre-determined value of film thickness all the time ensuring that the surfaces are nearly parallel to each other. After the motor is turned on, due to the

geometry of the PDMS specimen fluid is drawn into the gap between the surfaces and the fluid exerts pressure on the PDMS surface. Now the load cell which is connected to the signal conditioning unit gives out the value of this load. A computer with the software LabVIEW will be used to monitor the value of the load given out by the load cell. This value can be compared to the value obtained by the numerical model at the same value of initial film thickness. A detailed view of the experimental test rig is present in Fig. 5.8. The motor is mounted tightly on the base plate with its shaft passing through the bowl with the help of a bearing. The bearing ensures a tight fit of the shaft and the bowl and facilitates the rotation of the motor shaft. Aluminum micrometer stages could also be seen in the experimental setup picture which allows precise control of the distance between the two conforming surfaces. The load cell will measure the load being acted on the adapting surface due to the pressure exerted by the fluid in between the surfaces.

The experimental test rig built for the purpose of testing of the surfaces is capable of varying the operating conditions like pressure acting on the surface and the velocity of the opposing surface. As discussed earlier, the test rig is also compact and the process of testing can be viewed from a microscope which makes the process of analyzing the results easier by providing access to the process from close levels. A microscope of 10x eyepiece and a 7x objective was purchased for the process specifically.

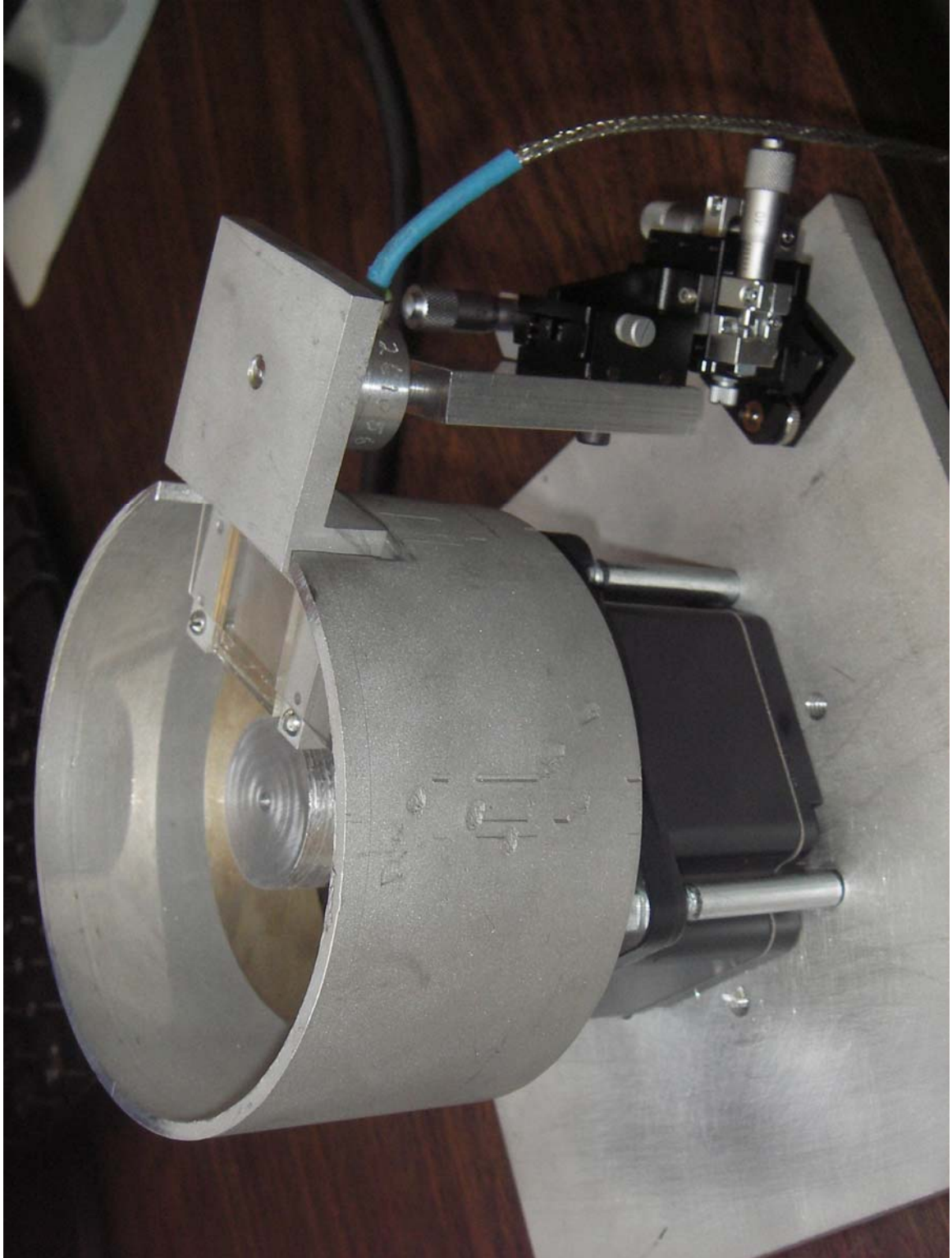


Figure 5.8: Photographic view of the experimental setup

CHAPTER 6

CONCLUSIONS

This work studies novel self-adapting micro-textures for hydrodynamic lubrication as a way of increasing their load carrying capacity when compared to their conventional counterparts. The self- adapting surfaces deform due to applied loads thereby adjusting their geometry to facilitate higher load carrying capacity of the surface. These surfaces would find use in the miniature components and systems where a high degree of precision is required.

The micro-textures are numerically modeled using the coupled equations of elasticity and hydrodynamic lubrication. The numerical modeling is done first so that it would provide a base to go into the experimental testing of these surface textures. Parametric studies were conducted which gave some insights into what to expect from the experimental testing and what the optimal geometrical parameters are. The pressure profile of the smart surface appeared similar to that of a sliding bearing case with minor differences. The optimum geometrical parameters to generate maximum load carrying capacity were found with the help of numerical modeling which can be used when fabricating the surfaces. It was found that load carrying capacity and pressure decrease with increase in minimum or initial film thickness. The load carrying capacity increases initially when the foil thickness is increased and after a certain critical value starts

decreasing. No load support is generated at higher values of film thickness and foil thickness. The film stiffness of the deforming self- adapting surface is greater than the static surface which does not deform.

A numerical model which can predict the load support for a certain minimum film height has been generated. The numerical model can be used as a basis for the experimental testing procedures and the results can be correlated to one another. This model can be used to optimize the geometry of the textures created for experimental purposes, as was done in this work. It was proved theoretically that the adapting surfaces perform better with higher load carrying capacity.

A specimen with the said micro textures was fabricated using micro fabrication techniques with Polydimethylsiloxane (PDMS). For the testing purposes a test rig was designed and built. Among the many features of the test rig, the ability to vary the operating conditions like microscale film thickness and velocity of the opposing surface are very useful to simulate the real time operating conditions and help to assess the performance of the self- adapting surfaces.

The availability of a microscope allows ensuring the parallel nature of the opposing surfaces and will be useful to view the surface behavior from close proximity. Viewing the process from close range would give an idea of the various phenomena occurring between the surfaces like cavitation. The test rig has a load cell to measure the amount of load acting on the surface. This would give an indication of the pressures being generated between the opposing surfaces and will be useful to regulate the load so that the self- adapting surface would not yield due to the prevalence of high loads.

6.1 Scope for future work

The current work solves the Reynolds equation for pressure by making it one dimensional by neglecting the side leakage or assuming that the pressure varies only in the sliding direction. A more accurate approach would be to solve a dynamic model accounting for pressure variation in the vertical direction or to solve the two dimensional Reynolds equation. In that case the pressure would be more accurate and close to the realistic values than the present work.

The material properties used in the current work are of Polydimethylsiloxane (PDMS) a polymer of silicon. In future a variety of materials can be used to fabricate the surfaces, each suitable for a specific application. For example materials like aluminum and copper can be used to fabricate the current micro textures discussed in this work to generate higher load support.

Although a test rig was designed and built for the purpose of conducting experiments on the fabricated self- adapting surfaces, they could not be completed due to lack of time. Experiments need to be conducted to ascertain the better performance of the self- adapting surfaces. In future interferometry techniques can be used to measure the film thickness accurately between the opposing surfaces.

REFERENCES

- [1] Hamilton, D. B., Walowit, J. A., and Allen, C. M., 1966, "A Theory of Lubrication by Microasperities," *ASME J. of Basic Engineering*, 88(1), pp. 177-185.
- [2] Jeng, Y.R., 1996, "Impact of Plateaued Surfaces on Tribological Performance," *Tribology Transactions*, 39(2), pp. 354-361.
- [3] Willis, E., 1986, "Surface Finish in Relation to Cylinder Liners," *Wear*, 109, pp.351-366
- [4] Etsion, I. and Burstein, L., (1996), "A Model for Mechanical Seals with Regular Microsurface Structure," *Tribology Transactions*, 39(3), pp. 677-683.
- [5] Etsion, I., Halperin G. and Greenberg, Y., 1997, "Increasing Mechanical Seal Life with Laser-Textured Seal Faces," 15th Int. Conf. On Fluid Sealing BHR Group, Maastricht, pp. 3-11.
- [6] Ronen, A., Etsion, I., and Kligerman, Y., 2001, "Friction-Reducing Surface Texturing in Reciprocating Automotive Components," *Tribology Transactions*, 44(3), pp. 359-366.
- [7] Ryk, G., Kligerman, Y., and Etsion, I., 2002, "Experimental Investigation of Laser Surface Texturing for Reciprocating Automotive Components," *Tribology Transactions*, 45(4), pp. 444-449.
- [8] Brizmer, V., Kligerman, Y., and Etsion, I., 2003, "A Laser Surface Textured Parallel Thrust Bearing," *Tribology Transactions*, 46(3), pp. 397-403.
- [9] Wang, X., Kato, K., and Adachi, K., 2002, "The Lubrication Effect of Micro-Pits on Parallel Sliding Faces of SiC in Water," *Tribology Transactions*, 45 (3), pp. 294-301.
- [10] Wang, X., Kato, K., Adachi, K., and Aizawa, K., 2003, "Loads Carrying Capacity Map for The Surface Texture Design of SiC Thrust Bearing Sliding in Water," *Tribology International*, 36(3), pp. 189-197.

- [11] Wang, X., Kato, K., Adachi, K., and Aizawa, K., The effect of laser texturing of SiC surface on the critical load for the transition of water lubrication mode from hydrodynamic to mixed. *Tribology International*, 2001. 34(10): pp. 703-711.
- [12] Etsion, I., Kligerman, Y. and Halperin, G., 1999, "Analytical and Experimental Investigation of Laser-Textured Mechanical Seal Faces," *Tribology Trans.*, 42(3), pp. 511-516.
- [13] Dumitru, G., Romano, V., Weber, H. P., Sentis, M., and Marine, W., 2003, "Ablation of Carbide Materials with Femtosecond Pulses," *Appl. Surf. Sci.*, 205, pp. 80-85.
- [14] Hoppermann, A., and Kordt, M., 2002, "Tribological Optimisation Using Laser-Structured Contact Surfaces," *O+P "Oelhydraulik und Pneumatik"*, 46(4), Vereinigte Fachverlage Mainz, ISSN 0341-2660.
- [15] Kligerman, Y. and Etsion, I., Analysis of the hydrodynamic effects in a surface textured circumferential gas seal. *Trib. Trans.*, 2001. 44(3): pp. 472-476.
- [16] Etsion, I., Kligerman, Y., and Halperin, G., Analytical and experimental investigation of laser-textured mechanical seal faces. *Trib. Trans.*, 1999. 42(3): pp. 511-516.
- [17] Kovalchenko, A., Ajayi, O., Erdemir, A., Fenske, G., and Etsion, I., The effect of laser texturing of steel surfaces and speed-load parameters on the transition of lubrication regime from boundary to hydrodynamic. *Trib. Trans.*, 2004. 47(2): pp. 299-305.
- [18] Etsion, I., Halperin, G., and Ryk, G. Improving tribological performance of mechanical components by laser surface texturing. in *ASTM Special Technical Publication*. 1999.
- [19] Etsion, I. and Halperin, G., A laser surface textured hydrostatic mechanical seal. *Trib. Trans.*, 2002. 45(3): pp. 430-436.
- [20] Etsion, I., 2005, "State of the Art in Laser Surface Texturing," *ASME J. Tribol.*, 127(1), pp. 248-253.
- [21] Etsion, I., Halperin, G., Brizmer, V., and Kligerman, Y., Experimental investigation of laser surface textured parallel thrust bearings, *Tribology Letters*, 17(2), pp. 295-300

- [22] H.L. Costa and I.M. Hutchings, Hydrodynamic lubrication of textured steel surfaces under reciprocating sliding conditions, *Tribology International*, Volume 40, Issue 8, August 2007, pp. 1227-1238.
- [23] Bulatov, V. P., Krasny, V. A., and Schneider, Y. G., 1997, "Basics of Machining Methods to Yield Wear and Fretting Resistive Surfaces, Having Regular Roughness Patterns," *Wear*, 208, pp. 132-137.
- [24] Komvopoulos, K., (2003), "Adhesion and Friction Forces in microelectromechanical Systems: Mechanisms, Measurement, Surface Modification Techniques, and Adhesion Theory," *J. Adhes. Sci. Technol.*, 17(4), pp. 477-517.
- [25] Wood, K.L., Neikirk, D., Busch-Vishniac, I., Weldon, W., Chu, C.-S., Kim, Y., Gupta, V., Maddox, W., and Masser, D., MEMs hydrodynamic bearings: Applications to and implications for machine failure prevention. *TriboTest*, 1998. 4(3): pp. 275-288.
- [26] Baroud C., Busch-Vishniac I., and Wood K., "Induced micro-variations in hydrodynamic bearings", *J of Tribol. -Trans. of ASME*, 2000. 122(3): pp. 585-589.
- [27] Jackson, R.L., Self Adapting Mechanical Step Bearings for Variations in Load. *Tribology Letters.*, 2005. 20(1): pp. 11-20.
- [28] Glavatskih, S., McCarthy, D., Sherrington, I., Hydrodynamic Performance of a Thrust Bearing with Micropatterned Pads. *Trib. Trans.*, 2005. 48(4): pp. 492-498.
- [29] Hearn, C., Maddox, W., Kim, Y., Gupta, V., Masser, D., Koeneman, P., Chu, C.S., Busch-Vishniac, I., Neikirk, D., Weldon, W., and Wood, K. Smart mechanical bearings using MEMS technology. in *American Society of Mechanical Engineers, Petroleum Division*. 1995.
- [30] Harp, S.R. and Salant, R.F., Inter-asperity cavitation and global cavitation in seals: An average flow analysis. *Tribology International*, 2002. 35(2): pp. 113-121.
- [31] Jacobson, B., Nano-meter film rheology and asperity lubrication. *J.of Tribology, Trans. ASME*, 2002. 124(3): pp. 545-550.
- [32] Shi, F. and Salant, R.F., Mixed soft elastohydrodynamic lubrication model with interasperity cavitation and surface shear deformation. *J. of Tribology, Trans. of ASME*, 2000. 122(1): pp. 308-316.

- [33] Shi, F. and Salant, R.F., Numerical study of a rotary lip seal with a quasi-random sealing surface. *J. of Tribol. -Trans. of ASME*, 2001. 123(3): pp. 517-524.
- [34] Lebeck, A.O., Parallel Sliding Load Support in the Mixed Friction Regime. Part 1 - The Experimental Data; Part 2 - Evaluation of the Mechanisms. *Journal of Tribology, Transactions of the ASME*, 1987. 109(1): pp. 189-205.
- [35] Wang, Q.J. and Zhu, D., Virtual texturing: Modeling the performance of lubricated contacts of engineered surfaces. *Journal of Tribology*, 2005. 127(4): pp. 722-728.
- [36] Ruan, B., Salant, R.F., and Green, I., Mixed lubrication model of liquid/gas mechanical face seals. *Tribology Transactions*, 1997. 40(4): pp. 647-657.
- [37] Shen, D. and Salant, R.F., Elastohydrodynamic analysis of the effect of shaft surface finish on rotary lip seal behavior. *Trib. Trans.*, 2003. 46(3): pp. 391-396.
- [38] Tonder, K. and Salant, R., Non-leaking lip seals: A roughness effect study. *Journal of Tribology, Transactions of the ASME*, 1992. 114(3): pp. 595-599.
- [39] Williams, J.A., *Engineering Tribology*. 2000, New York: Oxford.
- [40] Jackson, R. L., The Effect of Scale Dependant Hardness on Elasto-plastic Asperity Contact between Rough Surfaces, 2006, *Tribology Transactions*, 49, 2, pp.135-150.
- [41] Jackson, R.L. and Green, I., Study of the tribological behavior of a thrust washer bearing. *Trib. Trans.*, 2001. 44(3): pp. 504-508.
- [42] Hamrock, B.J., *Fundamentals of Fluid Film Lubrication*. 1994, New York: Mcgraw-Hill, Inc.
- [43] Hsu, S.M., Nano-lubrication: Concept and design. *Tribology International*, 2004. 37(7): pp. 537-543.
- [44] James M. Gere and Stephen P. Timoshenko, *Mechanics of Materials*. 1995, Boston: PWS, Inc.
- [45] Unger, M.A., Chou, H.P., Thorsen, T., Scherer, A., and Quake, S.R., Monolithic Microfabricated Valves and Pumps by Multilayer Soft Lithography. *Science*, 2002. 288: pp. 113-116.
- [46] <http://web.mit.edu/6.777/www/matprops/pdms.htm>

- [47] Suzuki K, Kurita M (2004) A MEMS-based active-head slider for flying height control in magnetic recording. *JSME Int J B* 47(3):pp. 453–458
- [48] Juang, J. Y., and Bogy, D. B., 2005, “Controlled-Flying Proximity Sliders for Head-Media Spacing Variation Suppression in Ultralow Flying Air Bearings,” *IEEE Trans. Magn.*, 41(10), pp. 3052–3054.
- [49] Kurita M, Yamazaki T, Kohira H, Matsumoto M, Tsuchiyama R, Xu J, Harada T, Inoue Y, Su LZ, Kato K (2002) An active-head slider with a piezoelectric actuator for controlling flying height. *IEEE Trans Magn* 38(5):pp. 2102–2104
- [50] F. Chen, H. Xie and G. Fedder, A MEMS-Based Monolithic Electrostatic Microactuator for Ultra-Low Magnetic Disk Head Fly Height Control, in *IEEE Transactions on Magnetics*, Volume 37, Issue 4, pp. 1915-1918, July 2001.
- [51] Brittain, S.; Paul, K.; Zhao, X.-M. and Whitesides, G., Soft lithography and microfabrication, *Physics World* 1998(11), 31-36.
- [52] S.R. Jambovane, E.C. Duin, and J.W. Hong, Novel nanoliter scale fluidic system for protein kinetics, In Preparation

APPENDIX A

MATLAB CODE FOR GENERATING THE PRESSURE PROFILE

```
clc
clear all
% length of the bit
l=200*10^-6;
w=0.02;
o=1;
q=1;
s=160;
r=0.5;
g=10;
e=1;
H=8e-6;
D(1:s)=0.0;
x=0:1/(s-1):1;
nodx=length(x);
p(1:nodx,1)=0.1;
p(1:nodx,2)=0.1;
gr(1:nodx,:)=0;
for ss=1:1
g=[6 10 14 18];
q
o
I=((w*(g(o)*10^(-6))^3)/12);
E=0.8*10^6;
HH(q)=H;
h(1:s)=H+D;
% viscosity of water at 27 degrees
n=0.8592*10^-3;
% velocity considering 570 rpm
sp=1500;
rad=0.047625;
u=(2*pi*sp*rad)/60;
d=(-6*n*u*1);
% initial load in newton
```

```

Pi=1;
% initial deflection
X=0;
if(ss<2)&(q<2)
for i=1:(r*s)
    A=0;
    deflect=0;
    for j=1:(r*s)
        B=((r)-A);
        if (X-A)<=0
            R=0;
        else
            R=(X-A);
        end
        deflect=deflect-(
(Pi*1^3/(6*E*I))*((B^2*X^3/(r^3))*(r+2*A)-
(3*A*B^2*X^2)/(r^2))-R^3));
        A=A+(1/s);
    end
    D(i)=deflect;
    X=X+(1/s);
    h(i)=H+D(i);
end
for i=(r*s):s
    for j=(r(e)*s):s
        B=1-A;
        deflect=0;
        A=A+(1/s);
    end
    D(i)=deflect;
    X=X+(1/s);
    h(i)=H+D(i);
end
oldD=D;
end
% loop to calculate pressure with h
lim=1;
while (lim>0.00001)
t=1;
NC=0;
while (t>0.00001)
    NC=NC+1;
p(s/40,2)=0;
for i= 1: s
    if (i==1)
        A=((h(i)+h(i+1))/2)^3;
        B=((h(nodx)+h(i))/2)^3;
        F=((h(i+1)-h(nodx))/2);
        G=A+B;
        p(i,2)=(1/G)*((d*(1/(s-
1)))*F)+(p(i+1,2)*A)+(p(nodx,2)*B));
        if p(i,2)<0
            p(i,2)=0;

```



```

end
elseif (i==s)
    A=((h(i)+h(1))/2)^3;
    B=((h(i-1)+h(i))/2)^3;
    F=((h(1)-h(i-1))/2);
    G=A+B;
    p(i,2)=(1/G)*((d*(1/(s-1))*F)+(p(1,2)*A)+(p(i-
1,2)*B));
    if p(i,2)<0
        p(i,2)=0;
    end
else
    A=((h(i)+h(i+1))/2)^3;
    B=((h(i-1)+h(i))/2)^3;
    F=((h(i+1)-h(i-1))/2);
    G=A+B;
    p(i,2)=(1/G)*((d*(1/(s-1))*F)+(p(i+1,2)*A)+(p(i-
1,2)*B));
    if i==(s/40)
        p(i,2)=0;
    end
    if p(i,2)<0
        p(i,2)=0;
    end
end
end
end
t=0;
tave=0;
for i=2:s
    tave=tave+p(i,1);
end
tave=tave/s;
for i=2:s
    t=t+abs((p(i,2) - p(i,1))/tave);
end
t;
p(:,1)=p(:,2);
end % inner while ends here
rf=(1/sqrt(NC)+.2)*abs(sin(NC/100));
if(rf>1)
    rf=1;
end

rf=0.25;
gr=p(:,1)*rf+gr*(1-rf);
% calculating area on which pressure is acting
c=(1/s)*l*w;
% pressure is multiplied by area to give force
P=c*gr;
% calculating the deflection
X=0;
if(ss<2) | (q<2)
for i=1:(r*s)

```

```

A=0;
deflect=0;
for j=1:(r*s)
    B=((r)-A);
    if (X-A)<=0
        R=0;
    else
        R=(X-A);
    end
    deflect=deflect-(
(P(j)*1^3/(6*E*I))*(((B^2*X^3/(r^3))*(r+2*A)-
(3*A*B^2*X^2)/(r^2))-R^3));
    A=A+(1/s);
end
D(i)=deflect;
X=X+(1/s);
h(i)=H+D(i);
end
for i=(r*s):s
    for j=(r*s):s
        B=1-A;
        deflect=0;
        A=A+(1/s);
    end
    D(i)=deflect;
    X=X+(1/s);
    h(i)=H+D(i);
end
end
X=x(1:s);
newD=D;
lim=0;
aveD=0;
for z=2:r*s
    aveD=aveD+newD(z);
end
aveD=aveD/(r*s-1);
for z=2:r*s
    lim=lim+abs((newD(z)-oldD(z))/aveD);
end
lim;
oldD=newD;
defmax(o)=max(oldD);
end %upper while ends here
pressure=p(:,2);
sum =0;
for i=1:s
    if (i==1) || (i==s)
        sum = sum + pressure(i)/6;
    elseif (mod(i,2)==0)
        sum = sum + 2*pressure(i)/3;
    else
        sum = sum + pressure(i)/3;
    end
end

```

```

    end
end
sum = sum*(2*l/s)*w;
% dividing by area for getting average pressure
avepres(o,q)=sum/(l*w);
dimlessload(o,q)=(l*avepres(o,q))/(6*n*u);
c=(gr*l/(6*n*u));
plot(X,c)
filmthicknessratio(o,q)=(HH(q)/(r(e)*l));
end % ss's for loop ends here
xlabel('Position, X');
ylabel('Dimensionless Pressure, P*');

```

APPENDIX B

MATLAB CODE FOR GENERATING THE DIMENSIONLESS LOAD PROFILE

```
clc
clear all
% length of the section
l=200*10^-6;
w=0.02;
o=1;
q=1;
s=160;
r=0.5;
g=10;
u=[2.5 5 7.5 10]
e=1;
H=1e-6;
D(1:s)=0.0;
x=0:1/(s-1):1;
nodx=length(x);
p(1:nodx,1)=0.1;
p(1:nodx,2)=0.1;
gr(1:nodx,:)=0;

for ss=1:1
    for o=1:4
        for q=1:19
            H=1e-6+(q-1)/4*2e-6
            HH(q)=H;
            h(1:s)=H+D;
        %end
    q
    o
    I=((w*(g*10^(-6))^3)/12);
    E=0.8*10^6;
    % viscosity of water at 27 degrees
    n=0.8592*10^-3;
    d=(-6*n*u(o)*l);
```

```

% initial load in newton
Pi=1;
% initial deflection
X=0;
if (ss<2)&(q<2)
for i=1:(r*s)
    A=0;
    deflect=0;
    for j=1:(r*s)
        B=((r)-A);
        if (X-A)<=0
            R=0;
        else
            R=(X-A);
        end
        deflect=deflect- (
(Pi*1^3/(6*E*I))*((B^2*X^3/(r^3))*(r+2*A) -
(3*A*B^2*X^2)/(r^2))-R^3));
        A=A+(1/s);
    end
    D(i)=deflect;
    X=X+(1/s);
    h(i)=H+D(i);
end
for i=(r*s):s
    for j=(r(e)*s):s
        B=1-A;
        deflect=0;
        A=A+(1/s);
    end
    D(i)=deflect;
    X=X+(1/s);
    h(i)=H+D(i);
end
oldD=D;
end
% loop to calculate pressure with h
lim=1;
while (lim>0.00001)
t=1;
NC=0;
while (t>0.00001)
    NC=NC+1;
p(s/40,2)=0;
for i= 1: s
    if (i==1)
        A=((h(i)+h(i+1))/2)^3;
        B=((h(nodx)+h(i))/2)^3;
        F=((h(i+1)-h(nodx))/2);
        G=A+B;
        p(i,2)=(1/G)*((d*(1/(s-
1)))*F)+(p(i+1,2)*A)+(p(nodx,2)*B));
        if p(i,2)<0

```

```

        p(i,2)=0;
    end
    elseif (i==s)
        A=((h(i)+h(1))/2)^3;
        B=((h(i-1)+h(i))/2)^3;
        F=((h(1)-h(i-1))/2);
        G=A+B;
        p(i,2)=(1/G)*((d*(1/(s-1))*F)+(p(1,2)*A)+(p(i-
1,2)*B));
        if p(i,2)<0
            p(i,2)=0;
        end
    else
        A=((h(i)+h(i+1))/2)^3;
        B=((h(i-1)+h(i))/2)^3;
        F=((h(i+1)-h(i-1))/2);
        G=A+B;
        p(i,2)=(1/G)*((d*(1/(s-1))*F)+(p(i+1,2)*A)+(p(i-
1,2)*B));
        if i==(s/40)
            p(i,2)=0;
        end
        if p(i,2)<0
            p(i,2)=0;
        end
    end
end
t=0;
tave=0;
for i=2:s
    tave=tave+p(i,1);
end
tave=tave/s;
for i=2:s
    t=t+abs((p(i,2) - p(i,1))/tave);
end
t;
p(:,1)=p(:,2);
end
rf=(1/sqrt(NC)+.2)*abs(sin(NC/100));
if(rf>1)
    rf=1;
end

rf=0.25;
gr=p(:,1)*rf+gr*(1-rf);
% calculating area on which pressure is acting
c=(1/s)*l*w;
% pressure is multiplied by area to give force
P=c*gr;
% calculating the deflection
X=0;
if(ss<2)|(q<2)

```

```

for i=1:(r*s)
    A=0;
    deflect=0;
    for j=1:(r*s)
        B=((r)-A);
        if (X-A)<=0
            R=0;
        else
            R=(X-A);
        end
        deflect=deflect- (
(P(j)*1^3/(6*E*I))*(((B^2*X^3/(r^3))* (r+2*A) -
(3*A*B^2*X^2)/(r^2))-R^3));
        A=A+(1/s);
    end
    D(i)=deflect;
    X=X+(1/s);
    h(i)=H+D(i);
end
for i=(r*s):s
    for j=(r*s):s
        B=1-A;
        deflect=0;
        A=A+(1/s);
    end
    D(i)=deflect;
    X=X+(1/s);
    h(i)=H+D(i);
end
end
X=x(1:s);
newD=D;
lim=0;
aveD=0;
for z=2:r*s
    aveD=aveD+newD(z);
end
aveD=aveD/(r*s-1);
for z=2:r*s
    lim=lim+abs((newD(z)-oldD(z))/aveD);
end
lim;
oldD=newD;
defmax(o)=max(oldD);
% calculation of new h
end
pressure=p(:,2);
sum =0;
for i=1:s
    if (i==1) || (i==s)
        sum = sum + pressure(i)/6;
    elseif (mod(i,2)==0)
        sum = sum + 2*pressure(i)/3;
    end
end

```

```

        else
            sum = sum + pressure(i)/3;
        end
    end
end
sum = sum*(2*l/s)*w;
% dividing by area for getting average pressure
avepres(o,q)=sum/(l*w);
dimlessload(o,q)=((l*avepres(o,q))/(6*n*u(o)));
aspectratio(o,q)=((g*10^-6)/(r(e)*l));
end
end
ylimit=((3*10^4*l)/(6*n*u(o)));
FF=ylimit;
for i= 1:4
    graph=dimlessload(:,i);
    plot(aspectratio(:,i),graph)
    hold on
end
plot(filmthicknessratio, dimlessload)
x=[HH(1) HH(15) HH(42) HH(65) HH(81)];
y=[FF FF FF FF FF ];
plot(x,y, '-r')
hold on
if(ss==1)
    plot(HH,dimlessload(1,:))
    hold;
else
    plot(HH,dimlessload(1,:), '-.');
end
end
xlabel('filmthicknessratio,h*');
ylabel('Dimensionless load carrying capacity, W');

```